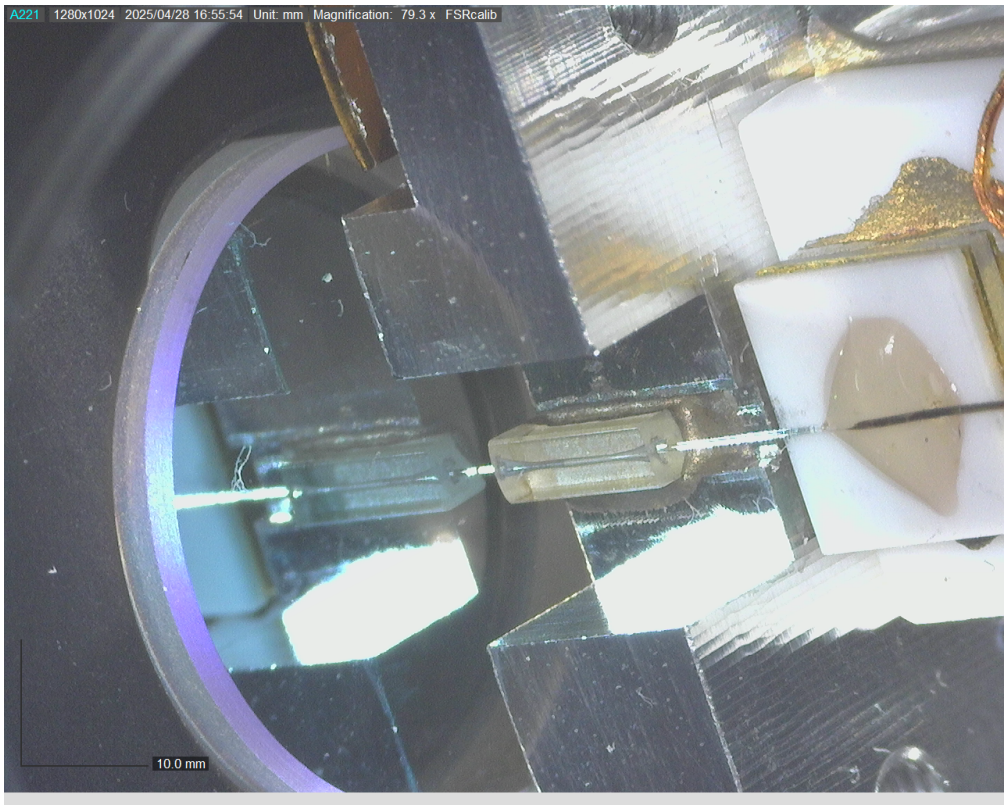

A vacuum integrated fibre Fabry-Pérot cavity setup for optical and optomechanical characterisation

Master's thesis in Physics

Johanna Örgård

DEPARTMENT OF MICROTECHNOLOGY AND NANOSCIENCE
CHALMERS UNIVERSITY OF TECHNOLOGY
Gothenburg, Sweden 2025
www.chalmers.se

Master's thesis 2025

A vacuum integrated fibre Fabry-Pérot cavity setup for optical and optomechanical characterisation

Johanna Örgård

CHALMERS
UNIVERSITY OF TECHNOLOGY

Department of Microtechnology and Nanoscience
Quantum Technology Laboratory
Quantum Sensing and Foundations Lab
Chalmers University of Technology
Gothenburg, Sweden 2025

A vacuum integrated fibre Fabry-Pérot cavity setup for optical and optomechanical characterisation
Johanna Örgård

Supervisor: Hannes Pfeifer, Department of Microtechnology and Nanoscience - MC2
Examiner: Witlef Wieczorek, Department of Microtechnology and Nanoscience - MC2

Master's Thesis 2025
Department of Microtechnology and Nanoscience
Quantum Technology Laboratory (QTL)
Quantum Sensing and Foundations Lab
Chalmers University of Technology
SE-412 96 Gothenburg
Telephone +46 31 772 1000

Cover: Picture of a fibre Fabry-Pérot cavity in the vacuum integrated setup for optomechanical characterisation explained in Chapter 3.

Typeset in LaTeX
Printed by Chalmers Reproservice
Gothenburg, Sweden 2025

A vacuum integrated fiber Fabry-Pérot cavity setup for optical and optomechanical characterisation

Johanna Örgård
Department of Microtechnology and Nanoscience
Chalmers University of Technology

Abstract

Fibre Fabry–Pérot cavities are miniaturised Fabry–Pérot cavities integrated on optical fibres. Their small size, open mode volume and intrinsic integration with optical fibres make them well suited for optomechanical experiments in which one studies the interaction between light and mechanical motion. The short cavity length enables enhancement of the vacuum optomechanical coupling strength and the open mode volume allows for the easy insertion of mechanical resonators or other quantum systems directly into the cavity. These features make fibre Fabry–Pérot cavities suited for many applications such as levitation of nano particles and quantum-enhanced inertial and force sensing.

In this master's thesis, an experimental platform was developed with the goal to enable optical and optomechanical characterisation of fibre Fabry–Pérot cavities consisting of a fibre mirror and a reflective mechanical resonator on a chip. To this end, an existing experimental setup for optical characterisation was improved upon through automatisation and a vacuum-integrated setup for optomechanical experiments was built and tested.

The resulting experimental platform enables measurements of the resonance linewidth and free spectral range of fibre Fabry–Pérot cavities. Within the vacuum-integrated setup the cavity length can be locked to the drive laser. This setup will in future work be used for optomechanical experiments measuring the optomechanical coupling strength and controlling mechanical resonator modes utilising the optical spring effect and optomechanical damping.

Keywords: optomechanics, fibre Fabry–Pérot cavity, photonic crystal, distributed bragg reflector, nanoscience

Acknowledgements

I would like to thank Prof. Witlef Wieczorek for giving me the opportunity to work in such a supportive and stimulating research team and for giving me so much support during these past few months. I would also like to thank my supervisor Hannes Pfeifer for guiding through every step of this project and teaching me so much about this existing research field. I am grateful to the optomechanics team as a whole, including Anastasiia Ciers and Alexander Wolfgang Martin Jung, for always being there to answer any questions I have had and giving me so many new insights. Thank you to the rest of the people at the Quantum Sensing and Foundations Lab: Paul Nicaise, Achintya Paradkar, Fabian Resare, Alireza Hashemi and Somiya Islam Soke; you have all been very welcoming to me I have always felt like there was someone to turn to if I needed help.

Johanna Örgård, Gothenburg, June 2025

List of Acronyms

Below is the list of acronyms that have been used throughout this thesis listed in alphabetical order:

AC	alternating current
DBR	distributed Bragg reflector
DC	direct current
EOM	electro-optic modulator
FC/APC	angled physical contact for fibre patch cord
FFPC	fibre Fabry-Pérot cavity
FPC	Fabry-Pérot cavity
HV	high vacuum
PDH	Pound–Drever–Hall
SoF	side-of-fringe

Nomenclature

Below is the nomenclature of recurring parameters and variables used throughout this thesis.

$\hat{a}$	photon annihilation operator
$\hat{a}^\dagger$	photon creation operator
$\hat{a}_{\mathrm{in}}$	the stochastic quantum field incident on the incoupling mirror
$\hat{a}_{\mathrm{out}}$	the field reflected from a Fabry-Pérot cavity
$\mathcal{A}$	parameter for the lineshape of the reflection from a FFPC
$\hat{b}$	phonon annihilation operator
$\hat{b}^\dagger$	phonon creation operator
c	speed of light
$\hat{f}_{\mathrm{in}}$	the stochastic quantum field incident on other incoupling channels than $\hat{a}_{\mathrm{in}}$
$\mathcal{F}$	finesse of an optical cavity
$F(\omega)$	complex reflection amplitude at an optical cavity
G	optical frequency shift per mechanical displacement
g_0	vacuum optomechanical coupling strength
g	$g = g_0\sqrt{\bar{n}_{\mathrm{cav}}}$, light-enhanced optomechanical coupling strength
$\hbar$	Planck's constant
L_{cav}	cavity length
m_{eff}	effective mass of mechanical resonator
$\bar{n}_{\mathrm{cav}}$	average number of photons circulating in an optical cavity
N	translational mode number of optical cavity
P_{in}	the power incident on the optical cavity
$P_{\mathrm{out}} = P_{\mathrm{ref}}$	the power reflected back from the optical cavity
$\mathcal{Q}_{\mathrm{opt}}$	optical quality factor
$\mathcal{Q}_{\mathrm{m}}$	mechanical quality factor
$\mathcal{S}_\epsilon$	noise spectral density for the error signal for a cavity lock

$\mathcal{S}_{\nu\nu}$	noise spectral density for the cavity resonance frequency ν_{cav}
$x(t)$	global amplitude of mechanical motion
x_{ZPF}	zero-point fluctuation amplitude of mechanical resonator
β	amplitude of the EOM signal
Γ_{m}	mechanical damping rate
Γ_{opt}	damping of the mechanical oscillator due to radiation pressure forces
Δ	$\Delta = \omega - \omega_{\mathrm{cav}}$, laser detuning with respect to the cavity mode
$\delta\Omega_{\mathrm{m}}$	shift of mechanical frequency resulting from optical spring effect
ϵ	the error signal for a cavity lock
η_{dip}	parameter expressing the resonance depth of FPCs
η_{r}	parameter for the lineshape of the reflection from a FFPC
η_{L}	parameter for the lineshape of the reflection from a FFPC
κ	full cavity decay rate
κ_{ex}	cavity decay rate due to transmission through the incouplng mirror
κ_{in}	cavity decay rate which is not due to transmission through the incouplng mirror
λ_{cav}	wavelength of a mode inside an optical cavity
ν_{FSR}	Free spectral range in terms of frequencies, equal to ω_{FSR}
ν_{cav}	frequency of a mode inside an optical cavity, equal to $\omega_{\mathrm{m}}/2\pi$
ν	$\nu = (\omega - \omega_{\mathrm{cav}})/\kappa$, variable expressing the lineshape of the reflection from a FFPC or FPC
ν_{laser}	frequency of the main tone of the laser drive, equal to $\omega/2\pi$
ν_{laser1} and ν_{laser2}	frequencies of the sideband tones
τ	average lifetime of a cavity photon
ω_{cav}	angular frequency of a mode inside an optical cavity
ω_{FSR}	Free spectral range in terms of angular frequencies
ω	angular frequency of the laser
Ω_{m}	angular frequency of mechanical resonator
Ω	angular frequency of the EOM signal

Contents

List of Figures

1

Introduction

In cavity optomechanics, one studies the interaction between the light in an optical cavity and mechanical motion. Optical cavities coupled to mechanical systems have many potential applications such as quantum-enhanced inertial and force sensing [1]. They can also be used to create non-classical states of light and mechanics as well as entangled states of light [2]. Furthermore, cavity optomechanics has been proposed as a key technology to establish long distance links in quantum information networks, for example by interconverting information stored in microwave domain solid-state qubits with information stored in flying photonic qubits [3].

One type of system used to achieve an optomechanical interaction is fibre Fabry–Pérot cavities (FFPCs). FFPCs are miniaturised Fabry–Pérot cavities (FPCs) integrated on optical fibres. They offer many advantages over classic FPCs such as intrinsic integration with optical fibres. In addition, their small size allows for reduction of the cavity length, which enhances the optomechanical coupling strength [3, 4]. FFPCs also have advantages over other platforms of similar or smaller size, such as whispering gallery mode resonators or optomechanical crystals. FFPCs can have larger intra cavity photon numbers without facing issues due to heating or thermal instability [5]. Additionally, the open mode volume of FFPCs allows for the easy insertion of other systems, such as membranes or levitated nano particles, to act as the mechanical element.

1.1 Goal and objectives

This masters thesis tackled the experimental realisation of a FFPC-based optomechanical testing platform in the "Quantum sensing and foundations lab" at Chalmers. The goal of this testing platform was to enable optical characterisation of, and optomechanical experiments with, FFPCs consisting of a fibre mirror and a reflective structure on a chip, see Figure 1.1. In the optomechanical experiments, these reflective structures take the form of mechanical resonators. The testing platform would enable manipulation and high precision read-out of their vibrational modes through optomechanical interaction with light in the cavity. To achieve this, an existing experimental setup for the optical characterisation of FFPCs was improved upon by automating the measurements using Python. This was then used to characterise some FFPCs by measuring the signal reflected from them and extracting their finesse.

In addition to this, an experimental setup was constructed to enable optical readout and control of on-chip mechanical resonators. This was integrated into a vacuum chamber so that the mechanical damping rate is not limited by the surrounding air. With this, initial test measurements where done to determine the amount of measurement noise in the setup and find ways to reduce it.

Chapter 2 of this report covers the theory which is necessary to understand FFPCs and the optomechanical experiments proposed in this thesis. Chapter 3 then explains the two experimental setups and the experiments they can be used for. Finally, Chapter 4 presents and discusses results of the experiments conducted with these setups.

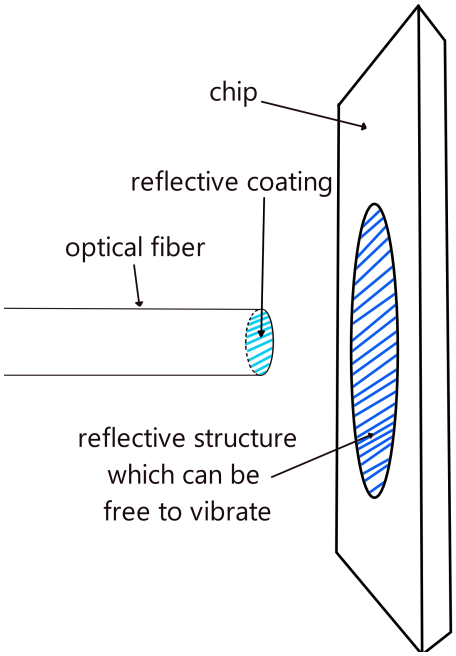

Figure 1.1: A conceptual sketch of a fibre Fabry-Pérot cavity that is explored in this thesis. It consists of a fibre mirror and a reflective structure on a chip.

2

Theory

This chapter introduces Fabry-Pérot cavities and Fibre Fabry-Pérot cavities, giving a basic theoretical framework and introducing relevant properties. Then, the basic concepts of cavity optomechanics will be introduced and some important consequences of optomechanical coupling in Fabry-Pérot cavities will be highlighted.

2.1 Fabry-Pérot cavities

A Fabry-Pérot cavity (FPC) is an optical cavity consisting of two highly reflective mirrors facing each other. Between the mirrors, light propagates in free space. The following introduction to the basic theory of FPCs and their properties will be based on [3]. A FPC contains a series of resonances with angular frequencies

$$\begin{aligned} \omega_{\text{cav, N}} = 2\pi\nu_{\text{cav, N}} &\approx \frac{N\pi c}{L_{\text{cav}}} \\ \Leftrightarrow N\lambda_{\text{cav,N}} &\approx 2L_{\text{cav}} \end{aligned} \tag{2.1}$$

where N is an integer that is called the mode number, L_{cav} is the distance between the mirrors and c is the speed of light in the medium between the mirrors. These resonances, or longitudinal modes, are separated in angular frequency by the free spectral range

$$\omega_{\text{FSR}} = \frac{\pi c}{L_{\text{cav}}} = 2\pi\nu_{\text{FSR}}. \tag{2.2}$$

An electromagnetic wave can only couple into a FPC if its frequency is close to some $\omega_{\text{cav,N}}$. To understand this, imagine an electromagnetic wave with another frequency being reflected back and forth between the mirrors. The waves travelling back and forth would cancel each other out due to destructive interference. An electromagnetic wave with angular frequency $\omega \approx \omega_{\text{cav,N}}$ that couples into a FPC will be reflected back and fourth between the mirrors and constructively interfering. this results in the field between the mirrors being stronger than the field coupling into the cavity. The enhancement of the electromagnetic power relative to the power coupled into the cavity is $\frac{1}{2\pi}$ times the finesse of the cavity

$$\mathcal{F} = \frac{\omega_{\text{FSR}}}{\kappa} \tag{2.3}$$

where κ is the cavity photon decay rate. κ is a measure of how quickly a photon leaves the cavity. This can happen via transmission through or absorption by the

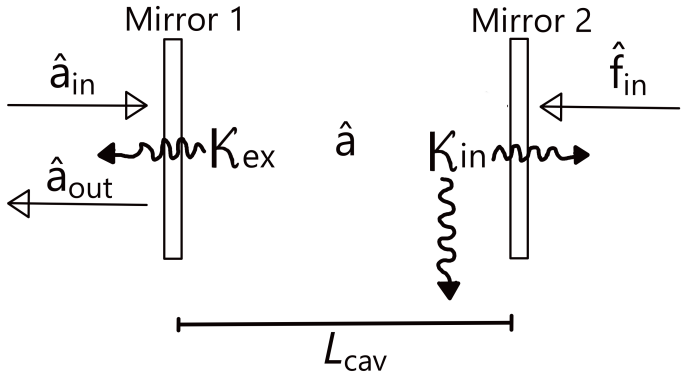

Figure 2.1: A conceptual sketch of Fabry-Pérot cavity with the cavity length L_{cav}. The fields in the input-output description of a FPC are illustrated. They are $\hat{a}$, the complex field amplitude of a mode inside the cavity, $\hat{a}_{\text{out}}$, the rate of light leaving the cavity from Mirror 1 and $\hat{a}_{\text{in}}$ and $\hat{f}_{\text{in}}$ which are the rates with which light arrives at Mirror 1 and Mirror 2 respectively. Also illustrated are the photon cavity decay rates, κ_{ex}, which describes the rate at which cavity photons leave the cavity out through Mirror 1, and κ_{in}, the decay rate associated with other channels.

mirrors and scattering out through the sides of the cavity. Note that κ can be defined differently in different texts, sometimes κ is defined such that $\mathcal{F} = \frac{\Delta\nu_{\text{FSR}}}{\kappa}$. Throughout this report κ is defined such that Equation 2.3 holds true. The optical quality factor of the cavity

$$\mathcal{Q}_{\text{opt}} = \omega_{\text{cav}}\tau, \tag{2.4}$$

where ω_{cav} is the angular frequency of the particular mode in question and $\tau = \frac{1}{\kappa}$ is the average lifetime of a cavity photon, measures how well the cavity confines energy. As the average time before a photon leaves the cavity is

$$\tau = \frac{1}{\kappa} = \frac{\mathcal{F}L_{\text{cav}}}{\pi c} \tag{2.5}$$

and the time it takes for a photon to travel once back and forth in the cavity is

$$\tau_R = \frac{2L_{\text{cav}}}{c}, \tag{2.6}$$

the average number of trips back and forth that a photon does before leaving the cavity is

$$\frac{\tau}{\tau_{\text{R}}} = \frac{\mathcal{F}}{2\pi} \tag{2.7}$$

which is the enhancement of electromagnetic power for the intra-cavity field.

One often needs to distinguish between energy leaving the cavity in ways necessary for measurements and energy leaving the cavity through other, often unwanted, channels. In this project, single-sided cavities are used, that is to say cavities where light is coupled into the cavity through Mirror 1, see Figure 2.1, and transmission out through Mirror 2 is not measured. The photon cavity decay rate due to transmission through the incoupling Mirror 1 is monitored and will be referred to as κ_{ex}. The rest of κ, including scattering out through the sides of the cavity, absorption by both mirrors and transmission through Mirror 2 will here be referred to as $\kappa_{\text{in}} = \kappa - \kappa_{\text{ex}}$.

2.1.1 Input-output theory for FPCs

Light in an optical cavity can be described like a driven harmonic oscillator by input-output theory. Consider the situation where a field from a coherent, monochromatic free space laser with angular frequency ω couples into a one-sided cavity. Input-output theory describes the time evolution of the annihilation operator for the intra-cavity field, $\hat{a}$, by the Heisenberg equation of motion

$$\dot{\hat{a}} = -\frac{\kappa}{2}\hat{a} + i\Delta\hat{a} + \sqrt{\kappa_{\text{ex}}}\hat{a}_{\text{in}} + \sqrt{\kappa_{\text{in}}}\hat{f}_{\text{in}} \tag{2.8}$$

in a frame of reference which rotates with the laser frequency such that $\hat{a}_{\text{lab}} = e^{-i\omega t}\hat{a}$. Here $\Delta = \omega - \omega_{\text{cav}}$ is the laser detuning with respect to the cavity mode, $\hat{a}_{\text{lab}}$ is the annihilation operator in the reference system of the lab and $\hat{a}$ is the same annihilation operator in the reference system that is assumed in Equation 2.8 which rotates relative to the lab. $\hat{a}^\dagger$ is the creation operator for the intra-cavity field and the two operators have the commutation relation

$$[\hat{a}, \hat{a}^\dagger] = 1. \tag{2.9}$$

$\hat{a}_{\text{in}}$ is a stochastic quantum field incident on Mirror 1, consisting of the laser field and the vacuum electric field coupling into the cavity through Mirror 1. $\hat{a}_{\text{in}}$ is defined such that $\langle\hat{a}_{\text{in}}^\dagger\hat{a}_{\text{in}}\rangle$ is the rate with which photons arrive at Mirror 1 meaning that the input power at Mirror 1 is

$$P_{\text{in}} = \hbar\omega\langle\hat{a}_{\text{in}}^\dagger\hat{a}_{\text{in}}\rangle, \tag{2.10}$$

Correspondingly, $\hat{f}_{\text{in}}$ refers to the field incident on any other incoupling channel such as Mirror 2 and the open sides of the cavity. The field reflected from the FPC is given by

$$\hat{a}_{\text{out}} = \hat{a}_{\text{in}} - \sqrt{\kappa_{\text{ex}}}\hat{a} \tag{2.11}$$

defined such that

$$P_{\text{out}} = \hbar\omega\langle\hat{a}_{\text{out}}^\dagger\hat{a}_{\text{out}}\rangle \tag{2.12}$$

is the power of the field going back from Mirror 1. See Figure 2.1 for a conceptual sketch of these fields. In this project, it is sufficient to go to the classical case by replacing $\hat{a}$ with its time average $\langle\hat{a}\rangle$ and similarly letting $\hat{a}_{\text{out}} \mapsto \langle\hat{a}_{\text{out}}\rangle$, $\hat{a}_{\text{in}} \mapsto \langle\hat{a}_{\text{in}}\rangle$ and $\hat{f}_{\text{in}} \mapsto \langle\hat{f}_{\text{in}}\rangle = 0$. In the classical case

$$\langle\hat{a}\rangle = \frac{\sqrt{\kappa_{\text{ex}}}\langle\hat{a}_{\text{in}}\rangle}{\kappa/2 - i\Delta} \tag{2.13}$$

is the steady state solution to Equation 2.8. The average number of photons circulating in the cavity is then given by

$$\bar{n}_{\text{cav}} = |\langle\hat{a}\rangle|^2 = \frac{\kappa_{\text{ex}}|\langle\hat{a}_{\text{in}}\rangle|^2}{\Delta^2 + (\kappa/2)^2} = \frac{\kappa_{\text{ex}}P_{\text{in}}}{[\Delta^2 + (\kappa/2)^2]\,\hbar\omega} \tag{2.14}$$

and the reflection amplitude at the cavity is given by

$$F(\omega) = \frac{\langle\hat{a}_{\text{out}}\rangle}{\langle\hat{a}_{\text{in}}\rangle} = \left(\langle\hat{a}_{\text{in}}\rangle - \frac{\kappa_{\text{ex}}\langle\hat{a}_{\text{in}}\rangle}{\kappa/2 - i\Delta}\right)/\langle\hat{a}_{\text{in}}\rangle = \frac{(\kappa_{\text{in}} - \kappa_{\text{ex}})/2 - i\Delta}{(\kappa_{\text{in}} + \kappa_{\text{ex}})/2 - i\Delta}. \tag{2.15}$$

For macroscopic FPCs that are coupling to free space light, the power reflected back from the cavity is then given by

$$P_{\text{out}}(\omega) = \hbar\omega|\langle\hat{a}_{\text{out}}\rangle|^2 = |F(\omega)|^2 P_{\text{in}} \tag{2.16}$$

if the incident field is mode matched to the cavity field. When $\Delta \ll \omega_{\text{FSR}}$,

$$|F(\omega)|^2 = \frac{P_{\text{out}}(\omega)}{P_{\text{in}}} = 1 - \eta_{\text{dip}}\frac{1}{1+\nu^2} \tag{2.17}$$

where $\nu = \Delta/\kappa = (\omega - \omega_{\text{cav}})/\kappa$ [6]. η_{dip} depends on the fraction $\frac{\kappa_{\text{ex}}}{\kappa_{\text{in}}}$ and reaches its maximum for critical coupling, $\kappa_{\text{ex}} = \kappa_{\text{in}}$. η_{dip} then decreases symmetrically for equally overcoupled ($\kappa_{\text{ex}} > \kappa_{\text{in}}$) and undercoupled ($\kappa_{\text{ex}} < \kappa_{\text{in}}$) cavities. η_{dip} further depends on the spatial mode matching efficiency at Mirror 1 which can be maximised by adjusting the relative alignment of the mirrors, maximising the resonance depth for a set value of $\frac{\kappa_{\text{ex}}}{\kappa_{\text{in}}}$, for more details see [6].

2.1.2 Fibre Fabry-Pérot cavities

Fibre Fabry–Pérot cavities (FFPCs) are miniaturised Fabry–Pérot cavities where one or both mirrors are on the facet of an optical fibre. The light coupling into the cavity is then not free space light, but fibre-guided light. They offer many advantages over classic FPCs such as high local field strength, small size, intrinsic integration with optical fibres and an open mode volume. They do however present some challenges compared to macroscopic FPCs. One such issue is that mechanical deformation of the fibre can cause noise when measuring the reflection from a FFPC. Another issue is that when measuring reflected power from a fibre end of a FFPC, $|F(\omega)|^2$ cannot be described by Equation 2.17. The reflection at FFPCs and its deviation from the classic FPCs described above is explored in [6]. The reason for this difference is that in order for the light reflected at a FFPC to reach a photodetector it needs to couple back into a guided mode of the fibre. Thus, the transverse mode shapes of the light in the cavity and fibre need to be considered. The problem is analogous to a macroscopic free space FPC with a mode-filter between the cavity and the photodetector. The light from the cavity that does not couple into the guided mode of the fibre is lost to the fibre cladding and not recorded by the photodetector. As a result, the reflection from the FFPC becomes a sum of a Lorentzian function, similar to the macroscopic case, and a dispersive function which amounts to

$$|F(\nu)|^2 = \frac{P_{\text{out}}(\nu)}{P_{\text{in}}} = \eta_r - \eta_L\left(\frac{1}{1+\nu^2} - \mathcal{A}\frac{\nu}{1+\nu^2}\right) \tag{2.18}$$

see Figure 2.2. η_{r}, η_{L} and $\mathcal{A}$ depend on the transverse spatial overlap amplitudes between the mode in the cavity and the guided mode of the fibre as well as between the mode directly reflected at the incoupling mirror and the guided mode of the fibre.

For a more in-depth description of η_{r}, η_{L} and $\mathcal{A}$ consider the forward and backward propagating spatial modes in the fibre, $|\psi_f^+\rangle$ and $|\psi_f^-\rangle$, and in the cavity, $|\psi_{\text{cav}}^+\rangle$ and

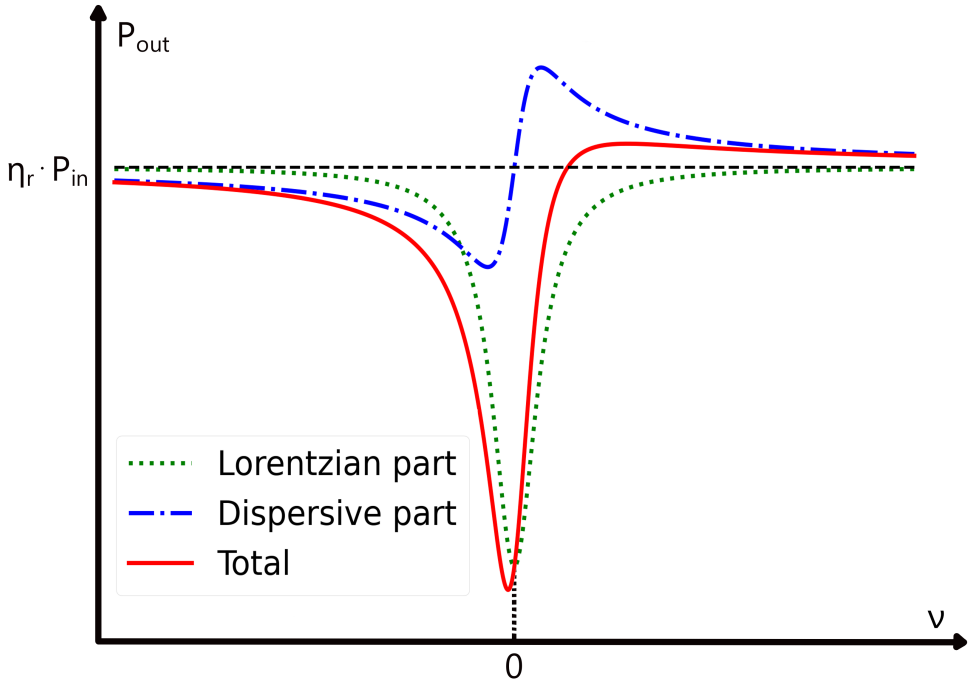

Figure 2.2: Sketch of the expected reflection signal from a FFPC based on Equation 2.18. The total reflected power (red line) is the sum of a Lorentzian part (dotted green line) and a dispersive part (dash-dotted blue line).

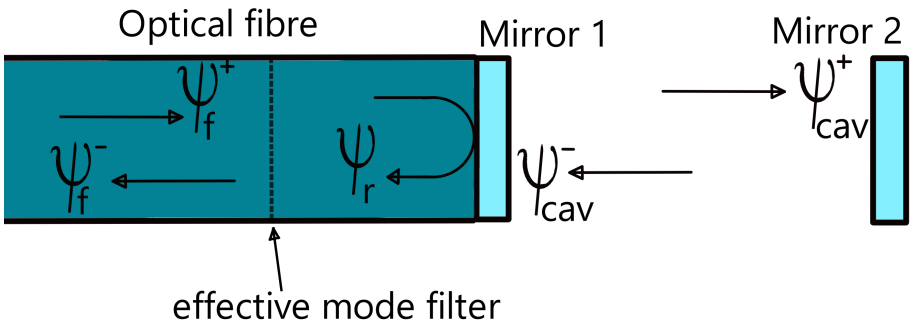

Figure 2.3: A conceptual sketch of a fibre Fabry-Pérot cavity illustrating the relevant spatial modes of light propagating in the fibre and the cavity.

$|\psi_{\text{cav}}^-\rangle$, together with the spatial mode of the reflection of $|\psi_f^+\rangle$ at Mirror 1, $|\psi_r\rangle$, see Figure 2.3. Following [6] one can define

$$\zeta = \langle \psi_{\text{cav}}^+ \,|\, \psi_f^+ \rangle \tag{2.19}$$

and

$$\xi = \langle \psi_f^- \,|\, \psi_r \rangle \tag{2.20}$$

and then notice that

$$\langle \psi_{\text{cav}}^- \,|\, \psi_r \rangle = \langle \psi_{\text{cav}}^+ | \mathbf{R}^\dagger \mathbf{R} | \psi_f^+ \rangle = \langle \psi_{\text{cav}}^+ \,|\, \psi_f^+ \rangle = \zeta, \tag{2.21}$$

where $\mathbf{R}$ is the operator for reflection at mirror 1, and

$$\langle \psi_{\text{cav}}^- \,|\, \psi_f^- \rangle = (\langle \psi_f^- \,|\, \psi_r \rangle)^* = \zeta^*. \tag{2.22}$$

It is then possible to show that

$$\eta_{\text{r}} = |\xi|^2, \tag{2.23}$$

$$\eta_{\text{L}} = \frac{4\mathcal{T}_1}{\mathcal{T}_1 + \mathcal{T}_2 + \mathcal{L}_1 + \mathcal{L}_2} \left(\text{Re}[\xi(\zeta^2)^*] - |\zeta|^4 \frac{\mathcal{T}_1}{\mathcal{T}_1 + \mathcal{T}_2 + \mathcal{L}_1 + \mathcal{L}_2} \right) \tag{2.24}$$

and

$$\mathcal{A} = \frac{\text{Im}[\xi(\zeta^2)^*]}{\text{Re}[\xi(\zeta^2)^*] - |\zeta|^4 \frac{\mathcal{T}_1}{\mathcal{T}_1 + \mathcal{T}_2 + \mathcal{L}_1 + \mathcal{L}_2}} \tag{2.25}$$

where $\mathcal{T}_{\text{i}}$ is the transmission coefficient for Mirror i and $\mathcal{L}_{\text{i}}$ is the losses for Mirror i due to absorption and scattering. Note that Equation 2.18 is not symmetric around $\nu = 0$ and that $|F(\nu)|^2$ does not reach its minimum for $\nu = 0$. Furthermore, the resonance depth for a FFPC (the depth of the reflection dip) is not maximised by maximising the mode matching efficiency between the cavity mode and the fibre guided mode, $|\zeta|^2$. The resonance depth can still be used as an approximation when aligning the cavity mirrors. For exact mode matching efficiencies, one would need to fit the reflection signal to Equation 2.18 and extract ζ and ξ from equations 2.23, 2.24 and 2.25.

2.2 Cavity optomechanics

Optomechanics is the study of how light interacts with mechanical motion through radiation pressure. This section will start with a brief background on mechanical resonators before explaining the optomechanical interaction in optical cavities based on derivations in [3].

2.2.1 Mechanical resonators

The theoretical description of vibrational movement is based on the linear theory of elasticity which describes vibrational movement in an object as a set of normal modes with corresponding frequencies [3]. The following description will focus on one normal mode with frequency Ω_{m}. The displacement of any part of the object is given by the displacement field $\vec{u}(\vec{r}, t) = x(t) \cdot \vec{u}(\vec{r})$ where the time-evolution of

the global amplitude of motion, $x(t)$, can be described as a harmonic oscillator with effective mass m_{eff} such that

$$m_{\text{eff}}\frac{dx^2(t)}{dt^2} + m_{\text{eff}}\Gamma_{\text{m}}\frac{dx(t)}{dt} + m_{\text{eff}}\Omega_{\text{m}}^2 x(t) = F_{\text{ex}}(t). \tag{2.26}$$

Γ_{m} is called the mechanical damping rate and can be expressed in terms of the mechanical quality factor

$$\mathcal{Q}_{\text{m}} = \Omega_{\text{m}}/\Gamma_{\text{m}} \tag{2.27}$$

and $F_{\text{ex}}(t)$ is the sum of all external forces acting on the mechanical oscillator. The energy of the mechanical oscillator is described by the Hamiltonian

$$\hat{H} = \hbar\Omega_{\text{m}}\hat{b}^\dagger\hat{b} + \frac{1}{2}\hbar\Omega_{\text{m}} \tag{2.28}$$

where $\hat{b}^\dagger$ and $\hat{b}$ are the phonon creation and annihilation operators such that

$$\hat{x} = \sqrt{\frac{\hbar}{2m_{\text{eff}}\Omega_{\text{m}}}}(\hat{b} + \hat{b}^\dagger) = x_{\text{ZPF}}(\hat{b} + \hat{b}^\dagger) \tag{2.29}$$

and

$$[\hat{b}, \hat{b}^\dagger] = 1. \tag{2.30}$$

x_{ZPF} is the zero-point fluctuation amplitude which describes the variance in position for the mechanical oscillator in the mechanical ground state, meaning that

$$\langle 0|\hat{x}^2|0\rangle = x_{\text{ZPF}}^2 \tag{2.31}$$

where $|0\rangle$ is the mechanical ground state.

2.2.2 Optomechanical coupling

Mechanical and optical modes can affect each other through various radiation-pressure forces [3]. This project concerns FFPCs where one of the cavity mirrors is on the facet of an optical fibre whilst the other takes the form of a reflective membrane on a chip which acts as a mechanical resonator. In such a system, the primary optomechanical interaction is the direct momentum transfer between photons and the mechanical resonator due to reflection. For such a system it is sufficient to first consider the Hamiltonian

$$\hat{H}_{\text{optomech.}} = \hbar\omega_{\text{cav}}(x)\hat{a}^\dagger\hat{a} + \hbar\Omega_{\text{m}}\hat{b}^\dagger\hat{b} \tag{2.32}$$

(here the zero-point energies are excluded since they do not affect the optomechanical coupling). The displacement of the vibrating mirror changes the length of the optical cavity, L_{cav}, and thus also the cavity frequency such that

$$\omega_{\text{cav}}(x) = \omega_{\text{cav}} + x\frac{\partial\omega_{\text{cav}}}{\partial x} + x^2\frac{\partial^2\omega_{\text{cav}}}{\partial x^2} + ... \tag{2.33}$$

where it is sufficient to keep only the linear term. Defining $G = -\frac{\partial\omega_{\text{cav}}}{\partial x}$ as the optical frequency shift per displacement, which for our simple case is $G = \frac{\omega_{\text{cav}}}{L_{\text{cav}}}$, the

Hamiltonian for the system containing a mechanical and optical resonator can be written as

$$\hat{H}_{\text{optomech.}} = \hbar(\omega_{\text{cav}} - G\hat{x})\hat{a}^\dagger\hat{a} + \hbar\Omega_{\text{m}}\hat{b}^\dagger\hat{b}. \tag{2.34}$$

In accordance with Equation 2.29 this can be written as

$$\hat{H}_{\text{optomech.}} = \hbar(\omega_{\text{cav}} - Gx_{\text{ZPF}}(\hat{b} + \hat{b}^\dagger))\hat{a}^\dagger\hat{a} + \hbar\Omega_{\text{m}}\hat{b}^\dagger\hat{b}. \tag{2.35}$$

The interaction part of the Hamiltonian is then

$$\hat{H}_{\text{int}} = -\hbar g_0\hat{a}^\dagger\hat{a}(\hat{b} + \hat{b}^\dagger) \tag{2.36}$$

where

$$g_0 = Gx_{\text{ZPF}} \tag{2.37}$$

is called the vacuum optomechanical coupling strength or the single-photon optomechanical coupling strength. Only considering Equation 2.36 the equations of motion for $\hat{a}$ and $\hat{b}$ would be the coupled differential equations

$$\dot{\hat{a}} = \frac{i}{\hbar}[\hat{H}_{\text{int}}, \hat{a}] = ig_0(\hat{b} + \hat{b}^\dagger)\hat{(a)} = iG\hat{x}\hat{a} \tag{2.38}$$

and

$$\dot{\hat{b}} = \frac{i}{\hbar}[\hat{H}_{\text{int}}, \hat{b}] = ig_0\hat{a}^\dagger\hat{a}. \tag{2.39}$$

In practice, both the cavity photons and the phonons of the mechanical resonator interact with more than just each other. The Hamiltonian describing the full system includes terms describing how energy is added into the cavity through a laser drive. It also includes phenomena such as photon cavity decay and mechanical damping as a result of the optical and mechanical resonators coupling to the rest of their environment. The effects on the optical mode from the full system is treated with input-output theory. In a reference system which, as described in Section 2.1.1, rotates with the laser frequency ω, input-output theory yields the full equation of motion for the optical field amplitude

$$\dot{\hat{a}} = -\frac{\kappa}{2}\hat{a} + i(\Delta + G\hat{x})\hat{a} + \sqrt{\kappa_{\text{ex}}}\hat{a}_{\text{in}} + \sqrt{\kappa_{\text{in}}}\hat{f}_{\text{in}} \tag{2.40}$$

by adding Equation 2.38 to Equation 2.8. $\hat{b}$, like $\hat{a}$, behaves as a harmonic oscillator and the equation of motion for $\hat{b}$ without optomechanical coupling is analogous to Equation 2.8, replacing κ with Γ_{m} and Δ with $-\Omega_{\text{m}}$. The full equation of motion for $\hat{b}$, including optomechanical coupling, then becomes

$$\dot{\hat{b}} = \left(-i\Omega_{\text{m}} - \frac{\Gamma_{\text{m}}}{2}\right)\hat{b} + ig_0\hat{a}^\dagger\hat{a} + \sqrt{\Gamma_{\text{m}}}\hat{b}_{\text{in}} \tag{2.41}$$

as long as $\Omega_{\text{m}} \gg \Gamma_{\text{m}}$, which can be assumed throughout this project. Both equations of motion are non-linear, with Equation 2.40 containing $\hat{x}\hat{a}$ and Equation 2.41 containing $\hat{a}^\dagger\hat{a}$. This makes cavity optomechanics a possible platform to study non-linear quantum effects. However, this requires large values for g_0 compared to κ. FFPCs is a possible platform for achieving higher values for g_0 because in a FPC

$$g_0 = Gx_{\text{ZPF}} = \frac{\omega_{\text{cav}}x_{\text{ZPF}}}{L_{\text{cav}}} = \frac{\omega_{\text{cav}}}{L_{\text{cav}}}\sqrt{\frac{\hbar}{2m_{\text{eff}}\Omega_{\text{m}}}} \tag{2.42}$$

and the small spatial dimensions of FFPCs make it possible to achieve small values for L_{cav}. Furthermore, as the cavity beam focus of a FFPC is small, it becomes possible to use small mechanical resonators with small m_{eff}. As of now, for most applications, it is sufficient to go to a linearised approximation of the interaction Hamiltonian

$$\hat{H}_{\mathrm{int}}^{(\mathrm{lin})} = -\hbar g_0 \sqrt{\bar{n}_{\mathrm{cav}}}(\delta\hat{a}^\dagger + \delta\hat{a})(\hat{b} + \hat{b}^\dagger) \tag{2.43}$$

where $\delta\hat{a} = \hat{a} - \langle\hat{a}\rangle = \hat{a} - \bar{\alpha}$ and $\bar{n}_{\mathrm{cav}} = \bar{\alpha}^2$ is the average number of photons circulating in the cavity.

Applying input-output theory to this linearised Hamiltonian (or approximating Equation 2.40 around a steady state $\bar{\alpha}$ by setting $\hat{a} = \bar{\alpha} + \delta\hat{a}$ and only keeping linear terms) yields the linear coupled equations of motion

$$\delta\dot{\hat{a}} = \left(i\Delta - \frac{\kappa}{2}\right)\delta\hat{a} + ig(\hat{b} + \hat{b}^\dagger) + \sqrt{\kappa_{\mathrm{ex}}}\delta\hat{a}_{\mathrm{in}}(t) + \sqrt{\kappa_{\mathrm{in}}}\hat{f}_{\mathrm{in}}(t) \tag{2.44}$$

and

$$\dot{\hat{b}} = \left(-i\Omega_{\mathrm{m}} - \frac{\Gamma_{\mathrm{m}}}{2}\right)\hat{b} + ig(\delta\hat{a} + \delta\hat{a}^\dagger) + \sqrt{\Gamma_{\mathrm{m}}}\hat{b}_{\mathrm{in}} \tag{2.45}$$

where $g = g_0\sqrt{\bar{n}_{\mathrm{cav}}}$ is the optomechanical coupling strength in the linearised regime. These linearised equations of motion are sufficient to explain the optomechanical effects that can be observed in the experiments constructed in this thesis.

2.2.2.1 The optical spring effect and optomechanical damping

Solving equations 2.44 and 2.45 in frequency space, and comparing the solution for the optomechanical coupled mechanical oscillator with equations expressing the behaviour of uncoupled mechanical oscillators, shows how the mechanical oscillator responds to the optomechanical coupling. The full derivation can be found in [3] and shows that for $\Delta \neq 0$, the laser drive shifts the frequency of the mechanical oscillator with

$$\delta\Omega_{\mathrm{m}}(\Omega_{\mathrm{new}}) = g^2\frac{\Omega_{\mathrm{m}}}{\Omega_{\mathrm{new}}}\left[\frac{\Delta + \Omega_{\mathrm{new}}}{(\Delta + \Omega_{\mathrm{new}})^2 + \kappa^2/4} + \frac{\Delta - \Omega_{\mathrm{new}}}{(\Delta - \Omega_{\mathrm{new}})^2 + \kappa^2/4}\right] \tag{2.46}$$

and adds a term

$$\Gamma_{\mathrm{opt}}(\Omega_{\mathrm{new}}) = g^2\frac{\Omega_{\mathrm{m}}}{\Omega_{\mathrm{new}}}\left[\frac{\kappa}{(\Delta + \Omega_{\mathrm{new}})^2 + \kappa^2/4} - \frac{\kappa}{(\Delta - \Omega_{\mathrm{new}})^2 + \kappa^2/4}\right] \tag{2.47}$$

to the damping of the mechanical oscillator so that the total damping becomes

$$\Gamma_{\mathrm{m,total}} = \Gamma_{\mathrm{m,intrinsic}} + \Gamma_{\mathrm{opt}}(\omega). \tag{2.48}$$

Here Ω_{m} is the original unperturbed mechanical frequency while Ω_{new} is the current mechanical frequency. In the, for this thesis, experimentally relevant limit of $\kappa \gg \Omega_{\mathrm{m}}$ (the so called unresolved-sideband regime) it is sufficient to approximate this around $\Omega_{\mathrm{new}} = \Omega_{\mathrm{m}}$ and these equations simplify to

$$\delta\Omega_{\mathrm{m}}|_{\kappa\gg\Omega_{\mathrm{m}}} = g^2\frac{2\Delta}{\kappa^2/4 + \Delta^2} = g_0^2\bar{n}_{\mathrm{cav}}\frac{2\Delta}{\kappa^2/4 + \Delta^2} \tag{2.49}$$

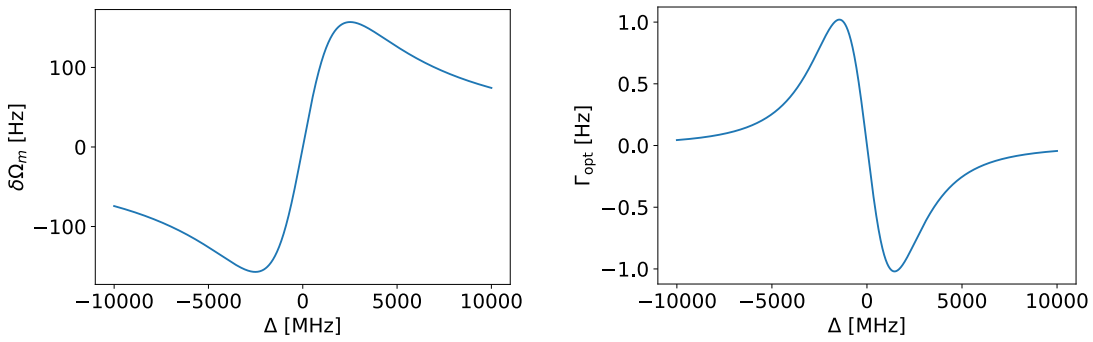

(a) **(b)**

Figure 2.4: Plot of $\delta\Omega_\mathbf{m}$ (a) and $\Gamma_\mathbf{opt}$ (b) as a function of laser detuning Δ when $\kappa \gg \Omega_\mathbf{m}$ for $g = 2\pi \cdot 100\,\mathrm{kHz}$, $\Omega_\mathrm{m} = 2\pi \cdot 1\,\mathrm{MHz}$ and $\kappa = 2\pi \cdot 800\,\mathrm{MHz}$.

and

$$\Gamma_\mathrm{opt}(\omega)|_{\kappa \gg \Omega_\mathrm{m}} = g^2 \left[\frac{\kappa}{(\Delta + \Omega_\mathrm{m})^2 + \kappa^2/4} - \frac{\kappa}{(\Delta - \Omega_\mathrm{m})^2 + \kappa^2/4} \right]. \tag{2.50}$$

See Figure 2.4 for some values for $\delta\Omega_\mathrm{m}|_{\kappa \gg \Omega_\mathrm{m}}$ and $\Gamma_\mathrm{opt}(\omega)|_{\kappa \gg \Omega_\mathrm{m}}$ as functions of detuning Δ. This shift of the mechanical frequency is called the optical spring effect and the shift in the damping is referred to as optomechanical damping (for $\Gamma_\mathrm{opt}(\omega) > 0$) or antidamping (for $\Gamma_\mathrm{opt}(\omega) < 0$).

3

Methods

The optomechanical testing platform developed in this master's thesis consists of two parts. Part one is an experimental setup which enables optical characterisation of FFPCs measuring their reflection and free spectral range. Part two is an experimental setup in high vacuum which enables optomechanical experiments using FFPCs and on-chip mechanical resonators. The FFPCs consists of a single mode optical fibre with a concave mirror on the facet and a chip with a reflective coating or reflective structures that are free to vibrate. The details of the two experimental setups are described in this chapter.

3.1 Optical characterisation of FFPCs

For optical characterisation under ambient conditions, an experimental setup and a Python-based control code was developed to measure finesse and coupling depth of FFPCs.

3.1.1 Experimental apparatus

An overview of the experimental setup is shown in Figure 3.1. First a laser tone is generated by a continuously tunable single-frequency diode laser. Three lasers[1] are available in the lab and are used depending on the desired wavelength range, together covering the range 1420-1620 nm. The laser light is coupled into fibre patch cord which passes through a paddle wheel polarisation controller to a phase modulating electro-optic modulator (EOM). The EOM is polarisation sensitive and the optimal polarisation depends on the wavelength of the light. The paddle wheel polarisation controller allows for the optimization of the polarisation going into the EOM. The EOM[2] is controlled by a signal generator[3] that adds a time dependent phase, $\varphi = \beta \sin \Omega t$, to the light going into the EOM. Thus, the signal exiting the EOM, which is the signal incident on the FFPC, becomes

$$E_{\text{inc}} = E_0 e^{i\omega t + i\beta \sin \Omega t}. \tag{3.1}$$

[1] CTL 1470, CTL 1500 and CTL 1550 from TOPTICA photonics controlled by digital laser controllers DLC pro from TOPTICA photonics

[2] MPZ-LN-10 from Exail

[3] SynthHD Mini

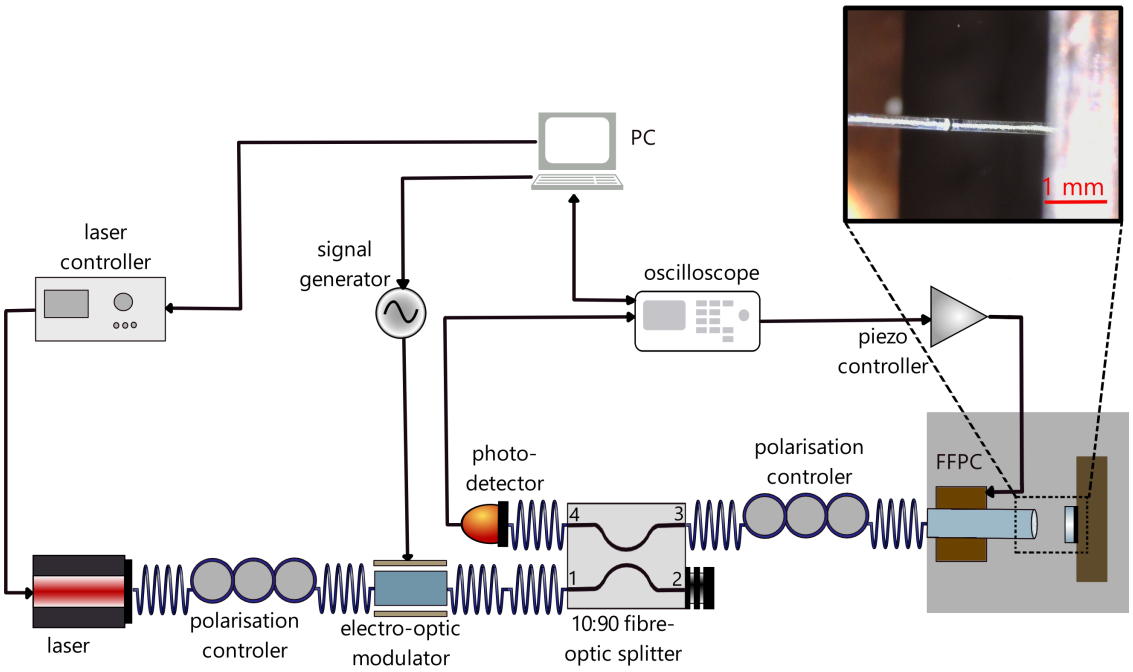

Figure 3.1: Overview of the setup for optical characterisation of FFPCs consisting of a continuously tunable laser source, that via single-mode optical fibre sends a signal through a paddle wheel polarisation controller to an electro-optic modulator, a 10:90 fibre-optic splitter, a photodetector and through another paddle wheel polarisation controller to the FFPC to be characterised. The fibre-end of the FFPC is mounted on a shear plate actuator. This enables continuous modulation of the cavity length by a piezo controller which in turn gets its signal from an oscilloscope. The other end of the FFPC consists of a chip that can be tilted and moved in any direction with micrometer precision, see Figure 3.2. The oscilloscope is also used to read out the signal from the photodetector.

According to [7], this expression can be expanded to first order using Bessel functions to

$$E_{\text{inc}} \approx E_0 \left[J_0(\beta) e^{i\omega t} + J_1(\beta) e^{i(\omega+\Omega)t} - J_1(\beta) e^{i(\omega-\Omega)t} \right]. \tag{3.2}$$

Consequently, the EOM adds two additional tones, called sidebands, to the light guided in the fibre, detuned by $\pm\Omega$ to the main tone. The sidebands and the main tone, is then led into Port 1 of a 10:90 fibre-optic splitter[4] with four ports, see Figure 3.1. 10% of the light exits the fibre-optic splitter at Port 3 and goes through another paddle wheel polarisation controller whilst the remaining 90% is lost to a beam dump at Port 2. This signal loss is compensated for by increasing the laser power. After the polarisation controller, the light is led into a copper coated single-mode optical fibre[5] with a convex mirror on its facet constituting one end of the FFPC. Port 4 of the fibre-optic splitter is coupled to a photodetector[6] which measures the signal reflected from the fibre-end of the FFPC. The reflected power is displayed on an oscilloscope[7] which can be interfaced with the computer.

The fibre-end with the mirror is mounted on a shear plate actuator[8], using a v-groove fibre holder[9], see Figure 3.2. The shear plate actuator enables continuous modulation of the cavity length by a piezo controller[10]. The output voltage of the piezo controller is modulated by a signal generated by the oscilloscope's wave generator output. The other end of the FFPC consists of a reflective structure on a chip that is mounted on a tiltable mirror mount that is in turn mounted on a micrometer translation stage[11]. The translation stage enables measurements on several parts of the chip. The tiltable mirror mount makes it possible to optimise the tilt of the chip for cavity alignment indicated by an optimal coupling of the optical mode in the fibre with the main optical mode of the cavity. A USB microscope[12] is used to get a visual image when adjusting the placement and tilt of the chip.

3.1.2 Data collection and analysis

The laser controller, radio frequency signal generator and oscilloscope are connected to a computer, enabling collection and analysis of data. The oscilloscope, through the piezo controller, applies voltage on the shear plate actuator as a sinusoidal function of time. The shear plate actuator subsequently puts the fibre end of the FFPC into a periodic forwards and backwards motion making the cavity length follow a periodic function in time. The amplitude of this curve is greater than half of the wavelength of the laser in air. This ensures that the cavity length at some point during the oscillation is such that the cavity is resonant with the laser. Around resonance, the reflection signal, measured with the photodetector, will have three dips as illustrated in Figure 3.3. The centre dip corresponds to the resonance of the main tone. On each side of this main dip there will be one additional dip that corresponds to the resonance for each of the sidebands created with the EOM. If

[4] FOBC-2-15-10-L-1-S-2 from AFW technologies
[5] Cu1300 from IVG
[6] PDA015C InGaAs amplified detector from Thorlabs
[7] EDUX1002G from Keysight
[8] NFL5DP20 from Thorlabs
[9] HFV001 from Thorlabs
[10] MDT693B from Thorlabs
[11] PT3 from Thorlabs
[12] Dino-lite digital microscope

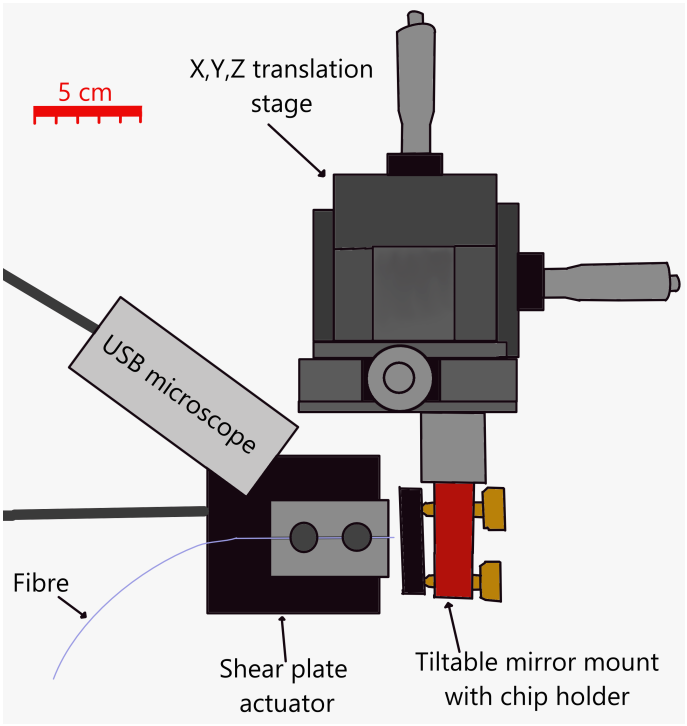

Figure 3.2: Sketch of the structure holding up and aligning the FFPCs during the optical characterisation. The fibre-end of the FFPC is mounted on a shear plate actuator, enabling continuous modulation of the cavity length. The other end of the FFPC consists of a chip that is mounted on a tiltable mirror mount that is in turn mounted on a micrometer translation stage.

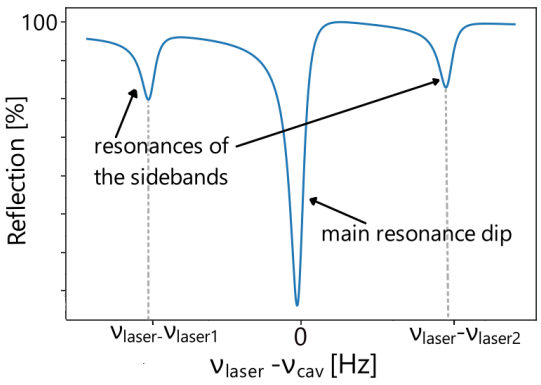

Figure 3.3: Sketch of the expected shape of the reflection signal around resonance. The signal features three dips, one from the main signal and two from the sidebands created with the EOM.

these dips occur when the movement of the fibre end can be approximated as linear then the time-axis is proportional to change in cavity length. This length can be expressed as $L_{\text{cav}} = L_o + \Delta L$ where L_o is the cavity length such that the cavity is resonant with the main tone of the laser. ΔL corresponds to a change in the resonance frequency of the cavity, $\delta\nu = \nu_{\text{laser}} - \nu_{\text{cav}}$, in accordance to

$$\begin{aligned} L_o &= \frac{Nc}{2\nu_{\text{cav}}} \\ \Rightarrow L_o + \Delta L &= \frac{Nc}{2(\nu_{\text{laser}} + \delta\nu)}. \end{aligned} \tag{3.3}$$

Close to resonance this can be expanded to

$$\begin{aligned} L_o + \Delta L &\approx \frac{Nc}{2}\left(\frac{1}{\nu_{\text{laser}}} + \frac{1}{\nu_{\text{laser}}^2}\delta\nu\right) \\ \Rightarrow \delta\nu &\approx \frac{2\nu_{\text{laser}}^2}{Nc}(L_o + \Delta L) - \nu_{\text{laser}} \end{aligned} \tag{3.4}$$

where N is the order of the cavity and c is the speed of light in the cavity medium. This is a linear function of ΔL which in turn is approximately a linear function of time. Therefore, as the frequency differences between the main signal and the sidebands are known, the sidebands facilitate the rescaling of the x-axis to the frequency domain. According to [6] the shape of one of these reflection dips can be described by Equation 2.18. The total reflective line shape can thus be described by

$$\begin{aligned} &\frac{P_{\text{out}}(\nu)}{P_{\text{in}}} = \eta_r - D_{\text{main}} - D_{\text{SB1}} - D_{\text{SB2}}, \text{ where} \\ &D_{\text{main}} = \eta_L\left(\frac{1}{1+\nu^2} - \mathcal{A}\frac{\nu}{1+\nu^2}\right), \\ &D_{\text{SB1}} = S_{\text{SB}}\eta_L\left(\frac{1}{1+\nu_{\text{SB1}}^2} - \mathcal{A}\frac{\nu_{\text{SB1}}}{1+\nu_{\text{SB1}}^2}\right) \text{ and} \\ &D_{\text{SB2}} = S_{\text{SB}}\eta_L\left(\frac{1}{1+\nu_{\text{SB2}}^2} - \mathcal{A}\frac{\nu_{\text{SB2}}}{1+\nu_{\text{SB2}}^2}\right). \end{aligned} \tag{3.5}$$

D_{main} corresponds to the dip in the reflected power that the resonance of the main tone gives rise to. D_{SB1} and D_{SB2} corresponds to the resonances with the sidebands. Therefore

$$\begin{aligned} \nu_{\text{SB1}} &= 2\pi(\nu_{\text{laser1}} - \nu_{\text{cav}})/\kappa \text{ and} \\ \nu_{\text{SB2}} &= 2\pi(\nu_{\text{laser2}} - \nu_{\text{cav}})/\kappa \end{aligned} \tag{3.6}$$

where ν_{laser1} and ν_{laser2} are the frequencies of the sidebands. S_{SB} is a scale factor between the main dip and the sideband dips owing to the fact that the main tone and the sidebands do not make up equal fractions of the total power transmitted in the fibre. The reflection data is fitted to Equation 3.5 using *SciPy* [8]. How the cavity length is regulated can cause distortions of the measured reflection signal. The data analysis described here assumes that L_{cav} changes as a linear function of time. In this project, L_{cav} was varied using a sinusoidal control signal for the shear

plate actuator and only measuring the finesse on reflection dips that occur when the voltage applied on the shear plate is within the middle 62.5 % of the voltage range in an attempt to stay within the relatively linear part of the sinus curve.

The visibility of the sideband dips can be optimised by changing the frequency of the sidebands with the EOM and changing the polarisation going into the EOM with the first paddle wheel polarisation controller. The second paddle wheel polarisation controller makes it possible to test if a frequency splitting of differently polarised cavity modes occurs for the reflection from the FFPC, for example due to a polarisation dependent reflection from the chip-surface.

The changing of wavelength with the laser controller as well as the process of retrieving data from the oscilloscope was automated using the application programming interface VISA (virtual instrument software architecture) via the *Python* libraries *toptica-lasersdk* [9] and *PyVISA* [10]. This makes it possible to quickly cycle through and measure κ for several wavelengths. If the reflective surface of the chip can be approximated as a plane mirror, this can further be used to identify the wavelength dependent reflection properties of the chip. The free spectral range, ν_{FSR}, of the FFPC is determined by recording the voltage applied to the shear plate actuator at resonance, "the resonance voltage", while changing the frequency of the main laser tone. As the cavity length is a function of this voltage, ν_{FSR} is the smallest non-zero difference in frequency between two laser signals with the same resonance voltage. κ and ν_{FSR} is then used to calculate the finesse, $\mathcal{F} = \frac{2\pi\nu_{\mathrm{FSR}}}{\kappa}$, at every wavelength step.

3.2 Optomechanical measurements

In order to perform optomechanical experiments with an FFPC, the cavity, the gray square in Figure 3.1, needs to be in high vacuum (HV). This is so that the quality factor of the mechanical resonator, as described in Section 2.2.1, is not limited by the damping from the surrounding air. To accomplish this, a FFPC setup was integrated into a HV chamber. In order to measure and control the frequency of the mechanical resonator as well as measure the optomechanical coupling strength, Pound-Drever-Hall (PDH) and side-of-fringe (SoF) locking were implemented. This section covers these locking techniques, how they were implemented in this project and how they can be used in optomechanical experiments.

3.2.1 Experimental apparatus

In order for the FFPC to be in vacuum, the shear plate actuator, tiltable mirror mount and translation stage is exchanged for vacuum compatible and remote controlled alternatives as shown in Figure 3.4. The chip is mounted onto a vacuum compatible, tiltable mirror mount[13]. The mirror mount is in turn mounted on two nanopositioners[14] that enable movement of the chip in the plane parallel to its sur-

[13] AG-M100 from Newport

[14] ECSx5050/StSt/NUM+/UHV from attocube

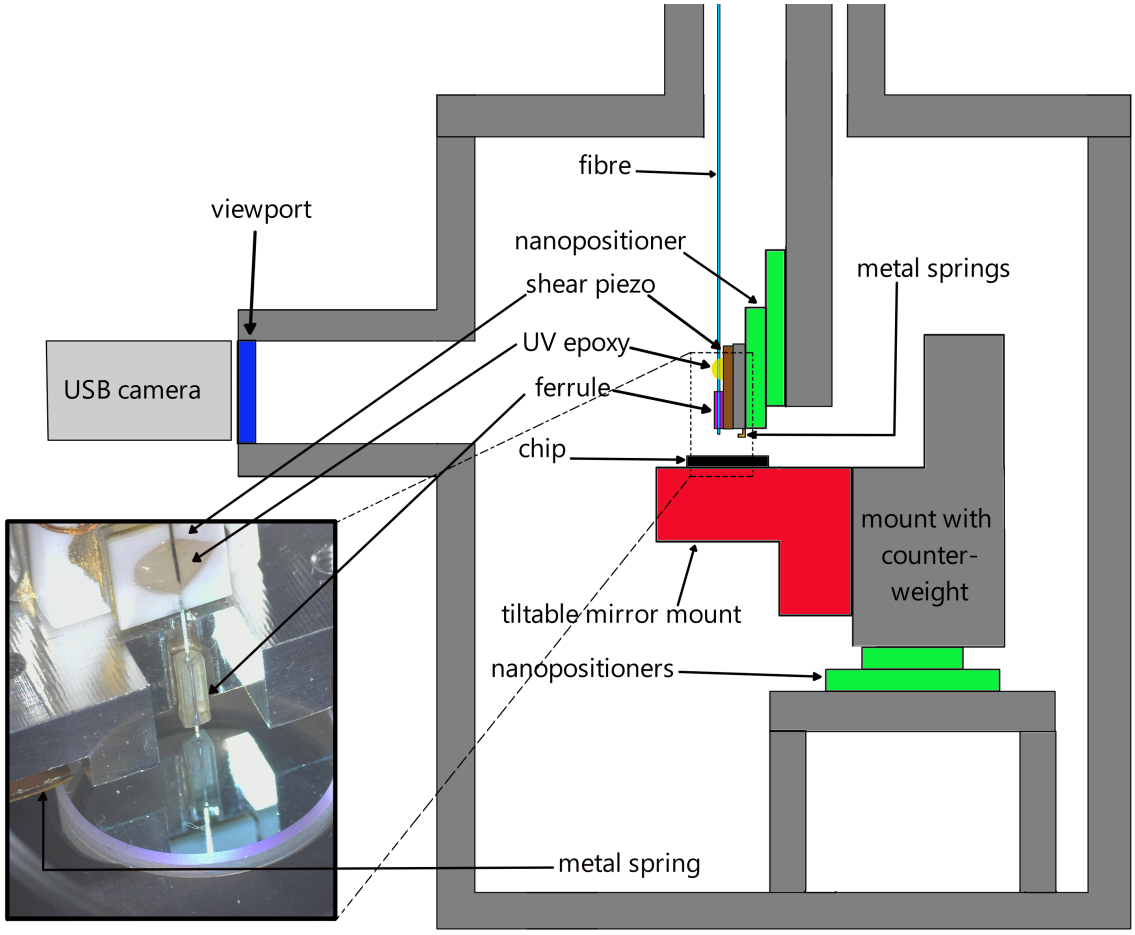

Figure 3.4: Sketch of a cross section of the vacuum chamber, showing the structure holding and aligning the FFPCs during the optomechanical experiments. The chip with the mechanical resonator is mounted on a tiltable mirror mount which is in turn mounted on top of two nanopositioners enabling movement of the chip in two dimensions. An aluminium holder was made to mount the mirror mount to the nanopositioners. The aluminium holder is designed such that the weight is equally distributed on the nanopositioners to avoid torque that might damage them. The fibre is mounted on a third nanopositioner enabling alignment of the cavity in the third dimension. On top of this nanopositioner, a shear piezo element is mounted which is used for fine-positioning of the fibre and thereby locking of the cavity. The fibre is glued to the shear piezo using UV epoxy. The position of the end of the fibre is stabilised in two dimensions by having it go through a glass ferrule. A USB microscope is mounted outside the vacuum chamber by a viewport, providing a visual image of the fibre and the chip with the help of a silver mirror (not shown in this sketch) which is mounted inside of the vacuum chamber. Also not shown in this sketch are wires sending signals to the tiltable mirror mount, nanopositioners and shear piezo connected to the outside through ports on the side of the chamber as well as the fibre feedthrough on the top of the chamber.

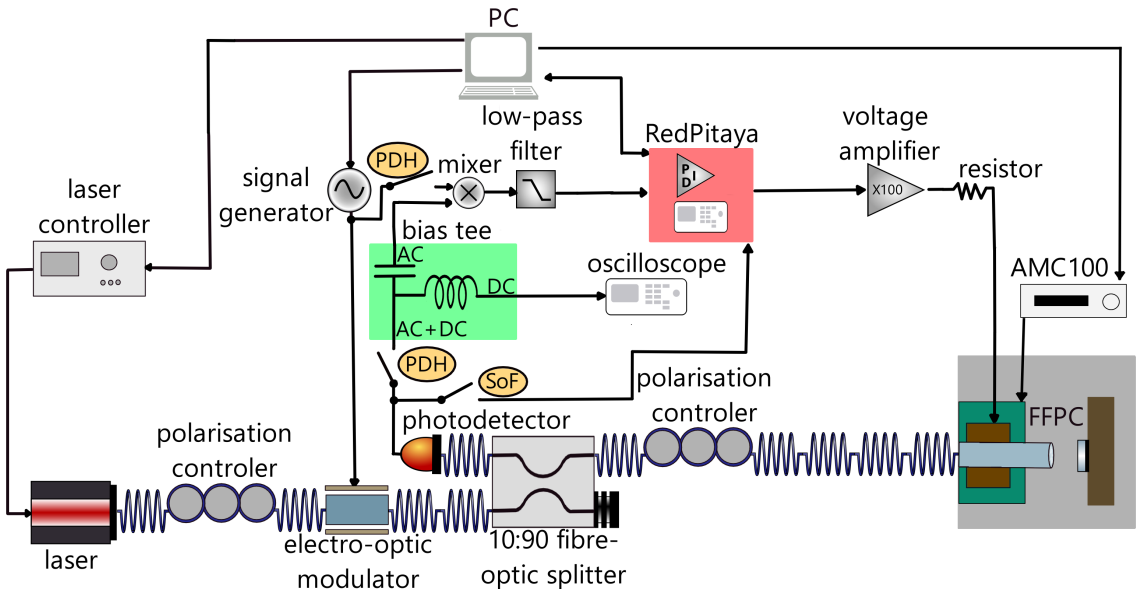

Figure 3.5: Overview of the setup for the optomechanical experiments consisting of the same optical components as in the setup for optical characterisation with some additional electrical components to enable the locking of the cavity length to the drive laser. These additional components are a multiplicative mixer, a low-pass filter, a resistor, a bias tee and a high-voltage amplifier and a RedPitaya. The three circuit breakers illustrate which path is used for PDH or SoF locking. The RedPitaya controls a shear piezo (here illustrated as a brown rectangle) used for fine positioning during PDH and SoF locking. A nanopositioner from Attocube (here illustrated as a dark green rectangle) controlled by an AMC100 is used to move the fibre along greater distances.

face. This is all mounted on the bottom of a HV chamber. A mounting post is attached to the top of the chamber. Attached at the bottom end of this mounting post is a slip-stick piezo-based nanopositioner[15] used to move the fibre end of the FFPC up and down. On top of the nanopositioning stage there is a holder with a shear piezo chip[16] on which the fibre is glued using UV epoxy. This shear piezo is controlled by the output from a voltage amplifier which in turn is controlled by the RedPitaya (a type of single-board computer) and used for fine positioning when scanning for resonances and for locking the cavity. The end of the fibre is going through a glass ferrule to stabilise it in two dimensions. For extra stabilisation in the third dimension, two metal springs are added at the end of the structure holding the fibre. During measurements, these springs are in contact with the chip holder, suppressing vibrations along the cavity axis that would otherwise change the cavity length. A USB microscope is mounted outside the vacuum chamber to provide a visual image of the inside.

Figure 3.5 shows an overview of the setup for the optomechanical experiments including the electrical components. The optical components are the same as for the

[15] ECSx3050/StSt/HL/NUM/HV controlled by an AMC100 from attocube

[16] PL5FBP3 from Thorlabs

optical characterisation described above. To enable SoF locking the RedPitaya was added to function as a proportional–integral–derivative (PID) controller and spectrum analyser. The RedPitaya is controlled using the open-source software *PyRPL* [11]. For the optomechanical experiments, the RedPitaya controls the oscillating piezo, here the shear piezo chip, instead of the oscilloscope and the piezo controller. Since the RedPitaya cannot put out higher voltage than 1 V a high-voltage amplifier[17] is added between the RedPitaya and the piezo chip, amplifying the voltage by a factor of 100. Additionally, a 18 kΩ resistor is added after the high-voltage amplifier. This resistor, together with the capacitance of the shear piezo chip, acts as a RC low-pass filter with a cutoff frequency of about 5.5 kHz that filters out the high frequency electrical noise from the RedPitaya. This noise would otherwise distort the reflection measurement by adding too much electrical noise to the control signal for the shear piezo chip. At the same time, the cut-off frequency for the filter cannot be too low as that would limit the lock bandwidth, making it unable to compensate for fast fluctuations in the cavity length. To determine the required resistor, a potentiometer, a type of variable resistor, was first used in its place. In the final setup however, the potentiometer is replaced with a normal resistor as the inductance of the potentiometer created a resonator circuit with the capacitance in the shear piezo chip, which distorted the reflection signal. To enable PDH locking, a multiplicative mixer[18] is added, mixing the signal from the photodetector with the control signal for the EOM. To the same end, a low-pass filter[19] is also added between the mixer and the RedPitaya. In addition to this, a bias tee[20] is added between the photodetector and the mixer, splitting the low frequency component of the reflection signal from the high frequency components relevant for the PDH locking. This enables simultaneous visualization of the reflection dip on the oscilloscope during PDH locking. Whether this mixer, low-pass filter and bias tee is used depends on which type of locking is to be used, this is illustrated with the three circuit breakers in Figure 3.5.

It is noted in [6] that optical interference along the fibre between the EOM and the cavity, as well as between the cavity and the photodetector, can cause drifts in the cavity lock. An example of such optical interference is reflection at the connection between the FFPC fibre and the rest of the fibre. In [6], they tested different alternatives for connecting these two fibres to minimise said reflection and found that the best result was achieved by fusion splicing the single mode FFPC fibre with commercially available FC/APC connected single mode fibres. In this project the FFPC fibre was similarly connected to FC/APC connected single mode fibres. To further minimise the optical interference along the beam path, the fibre was taped down onto the optical table where possible.

[17] A600 from pendulum
[18] ZX05-42MH-S+ from Mini-Circuits
[19] EF5.. from Thorlabs
[20] ZFBT-4R2GW+ from Mini-Circuits

3.2.2 Pound-Drever-Hall locking for optomechanical characterisation

The slope of the power of a signal reflected from a FFPC is approximately symmetric around resonance, see Figure 3.3. This means that looking only on the reflected power one cannot differentiate between the cavity being slightly too long and the cavity being slightly too short when trying to lock on resonance. Therefore, the reflected power cannot directly be used as an error signal when locking the cavity at resonance. This is solved by PDH locking. The PDH locking technique was originally designed to improve frequency stabilisation in lasers by locking the laser frequency to a stable Fabry-Pérot cavity but it can just as well be used to lock a Fabry-Pérot cavity to a stable laser signal, as will be shown through the following derivation based on [7]. As the expression in Equation 3.2 describes the light incident on the cavity, the light reflected at the fibre end of the cavity can be expressed as

$$E_{\text{ref}} = E_0 \left[F(\omega) J_0(\beta) e^{i\omega t} + F(\omega+\Omega) J_1(\beta) e^{i(\omega+\Omega)t} - F(\omega-\Omega) J_1(\beta) e^{i(\omega-\Omega)t} \right] \quad (3.7)$$

where $F(\omega)$ is the reflection coefficient at the cavity for light with angular frequency ω. The photodetector measures the reflected power

$$\begin{aligned} P_{\text{ref}} =& |E_{\text{ref}}|^2 = P_{\text{main}} |F(\omega)|^2 + P_{SB} \left\{ |F(\omega+\Omega)|^2 + |F(\omega-\Omega)|^2 \right\} \\ &+ 2\sqrt{P_{\text{main}} P_{\text{SB}}} \{ \text{Re}[F(\omega)F^*(\omega+\Omega) - F^*(\omega)F(\omega-\Omega)] \cos\Omega t \\ &+ \text{Im}[F(\omega)F^*(\omega+\Omega) - F^*(\omega)F(\omega-\Omega)] \sin\Omega t \} + (\text{terms with frequency } 2\Omega) \end{aligned} \quad (3.8)$$

where

$$P_{\text{main}} = J_0^2(\beta) |E_0|^2 \quad (3.9)$$

is the power of the incident main tone and

$$P_{\text{SB}} = J_1^2(\beta) |E_0|^2 \quad (3.10)$$

is the power of each of the incident sidebands. The signal from the photodetector is mixed with the control signal for the EOM, $\beta \sin\Omega t + \phi$ with a multiplicative mixer. Here ϕ represents the phase shift between the two signals due to unequal delays in the two signal paths. ϕ can be adjusted by cable length, a phase shifter or the choice of Ω to be $\phi = 0\,\text{rad}$ or $\phi = \pi/2\,\text{rad}$ so that the signal from the photodetector mixes with a pure $\sin\Omega t$ or a pure $\cos\Omega t$ signal. Then, since

$$\sin\Omega t \sin\Omega t = \frac{1}{2}(1 - \cos 2\Omega t), \quad (3.11)$$

$$\sin\Omega t \cos\Omega t = \frac{1}{2} \sin 2\Omega t \quad (3.12)$$

and

$$\cos\Omega t \cos\Omega t = \frac{1}{2}(1 + \cos 2\Omega t), \quad (3.13)$$

the signal exiting the mixer consists of a DC term and AC terms with the frequencies Ω and 2Ω. The AC signal is filtered out with the low-pass filter and what is left is

$$\epsilon = \sqrt{P_{\text{main}} P_{\text{SB}}} \text{Im}[F(\omega)F^*(\omega+\Omega) - F^*(\omega)F(\omega-\Omega)] \quad (3.14)$$

if $\phi = 0\,\text{rad}$ or

$$\epsilon = \sqrt{P_{\text{main}}P_{\text{SB}}}\text{Re}[F(\omega)F^*(\omega+\Omega) - F^*(\omega)F(\omega-\Omega)] \tag{3.15}$$

if $\phi = \pi/2\,\text{rad}$. Notice how the DC part of the reflected power, see in Equation 3.8, is filtered out with the mixer and low-pass filter before it reaches the RedPitaya. In other words, it does not affect the locking and might as well be used for something else. In this setup, the DC part of P_{ref} is diverted to the oscilloscope using a bias tee and used to visualise the reflection signal while locking. In the regime where $\Omega \ll \kappa$,

$$F(\omega)F^*(\omega+\Omega) - F^*(\omega)F(\omega-\Omega) \approx \frac{d|F(\omega)|^2}{d\omega}\Omega \tag{3.16}$$

which is purely real so $\phi = \pi/2$ is desired. The cavities in this project have a linewidth, $\kappa/2\pi$, on the order of GHz whilst $\Omega/2\pi \approx 300\,\text{MHz}$. Then

$$\epsilon \approx \sqrt{P_{\text{main}}P_{\text{SB}}}\frac{d|F(\omega)|^2}{d\omega}\Omega \approx \frac{P_{\text{in}}\beta}{2}\frac{d|F(\omega)|^2}{d\omega}\Omega \tag{3.17}$$

which would be linear around resonance and zero at the resonance frequency for a cavity whose reflection signal is symmetric around resonance. This makes it suitable as an error signal for a PID controller locking the cavity length of a FPC at resonance with a stable laser signal. Similar arguments can be made for when $\Omega \gg \kappa$.

When the cavity is locked to the laser, the mechanical resonator, making up the other mirror in the FFPC, will cause a periodic change in the cavity length which will cause a periodic change in the error signal. The frequency of this periodic change, $\Omega_{\text{m}}/2\pi \approx 1\,\text{MHz}$, will be far outside the locking bandwidth of the PID controller. Thus, this periodic change will cause a peak in the noise spectral density of ϵ, $\mathcal{S}_\epsilon$, at the frequency of the mechanical resonator, allowing one to measure it.

However, FFPCs are not symmetric and $\frac{d|F(\omega)|^2}{d\omega} \neq 0$ at resonance, see Section 2.1.2. So locking an FFPC with ϵ as error signal means that the cavity is blue-detuned and the mechanical resonator will be slightly spring hardened (see Equation 2.49) which affects the accuracy of the vibration measurements. To mitigate this, a bias, $\delta\epsilon$, is added to ϵ to form the error signal. This bias can be estimated as

$$\delta\epsilon \approx -\sqrt{P_{\text{main}}P_{\text{SB}}}\Omega\left.\frac{d|F(\omega)|^2}{d\omega}\right|_{\omega=\omega_{\text{cav}}} = -\sqrt{P_{\text{main}}P_{\text{SB}}}\Omega\frac{1}{|E_0|^2}\left.\frac{dP_{\text{ref}}}{d\omega}\right|_{\omega=\omega_{\text{cav}}} \tag{3.18}$$

using Equation 3.17. Then using Equation 2.18 where

$$\nu = 2\pi(\nu_{\text{laser}} - \nu_{\text{cav}})/\kappa = (\omega - \omega_{\text{cav}})/\kappa \tag{3.19}$$

to express the reflected power around resonance results in

$$\frac{1}{|E_0|^2}\left.\frac{dP_{\text{ref}}}{d\omega}\right|_{\omega=\omega_{\text{cav}}} = \frac{\eta_L}{\kappa}\left.\left(-\frac{2\nu}{(1+\nu^2)^2} - \mathcal{A}\frac{1-\nu^2}{(1+\nu^2)^2}\right)\right|_{\omega=\omega_{\text{cav}}} = -\frac{\eta_L\mathcal{A}}{\kappa}. \tag{3.20}$$

Thus

$$\delta\epsilon \approx \frac{P_{\text{in}}\beta\Omega\eta_L\mathcal{A}}{2\kappa}. \tag{3.21}$$

η_L, $\mathcal{A}$ and κ one obtains from fitting the reflection signal to Equation 2.18 as described in Section 3.1. To get a more accurate value for $\Delta\epsilon$ the fact that $\kappa \gg \Omega_\mathrm{m}$ is utilised. In this regime, $\delta\Omega_\mathrm{m}$, caused by the optical spring effect, is linearly dependent on $\bar{n}_\mathrm{cav}$, see Equation 2.49, and there by also on the power of the laser, see Equation 2.14. Thus, measuring the dependency that Ω_m has on the laser power for different biases, $\delta\epsilon$, and plotting this in a graph yields straight lines that bisect when the laser power approaches zero. The value for Ω_m where these lines bisect is the value for Ω_m unaffected by the optical spring effect. The bias that results in this value independently of the laser power is the exact bias to add to the error signal to lock the cavity at resonance.

When the cavity is locked, one can use the noise spectral density of ϵ for the locked cavity, $\mathcal{S}_\epsilon$, to extract the optomechanical coupling strength, g_0. According to [12, 13], the peak in the noise spectral density for the cavity resonance frequency, ν_cav, caused by the mechanical resonator can be expressed as

$$\mathcal{S}_{\nu\nu}(f) = \frac{2g_0^2\Omega_\mathrm{m}\Gamma_\mathrm{m}k_BT}{\pi^2\hbar\left[(\Omega_\mathrm{noise}^2 - \Omega_\mathrm{m}^2)^2 + \Gamma_\mathrm{m}^2\Omega_\mathrm{noise}^2\right]} \tag{3.22}$$

where $f = \Omega_\mathrm{noise}/2\pi$ is the noise frequency, $\Gamma_\mathrm{m}/2\pi$ is the mechanical linewidth, k_B is Boltzmann's constant and T is the temperature of the mechanical resonator. Getting g_0 is then a question of getting from $\mathcal{S}_\epsilon$ to $\mathcal{S}_{\nu\nu}$ and then fitting $\mathcal{S}_{\nu\nu}$ to Equation 3.22. The first step of getting from $\mathcal{S}_\epsilon$ to $\mathcal{S}_{\nu\nu}$ is to measure ϵ as a function of $\delta\nu = \nu_\mathrm{laser} - \nu_\mathrm{cav}$. Measuring ϵ as a function of time whilst changing the cavity length, one can get ϵ as a function of $\delta\nu$ the same way as in Section 3.1.2. Close to resonance, ϵ has an approximately linear dependency on $\delta\nu$. Therefore it is simple to extract $\frac{d\epsilon}{d\delta\nu}$ from the measurement after rescaling the time axis to the frequency domain. Then one can calculate

$$\mathcal{S}_{\nu\nu} = \mathcal{S}_\epsilon \left(\frac{d\epsilon}{d\delta\nu}\right)^{-2} \tag{3.23}$$

and fit its peak around $\Omega_\mathrm{noise} = \Omega_\mathrm{m}$ to Equation 3.22 to get g_0.

3.2.3 Side-of-fringe locking and the optical spring effect

In SoF locking, the cavity is locked to one of the slopes in the reflection signal on either side of resonance. In the middle of such a slope, the reflected power has an approximately linear dependence on a change in cavity length. This means that, for SoF locking, the reflected power is in itself suitable as an error signal for a PID controller. As such, the signal from the photodetector is led directly to the RedPitaya without passing the mixer or low-pass filter. Locking the cavity to the side of resonance causes a frequency shift in the mechanical resonator as expressed by Equation 2.46, and a change in the mechanical damping rate, as expressed by Equation 2.50 for standard optomechanical setups[21]. Figure 3.6 shows $\delta\Omega_\mathrm{m}$ and Γ_opt using equations 2.46 and 2.50 for $g_0 = 2\pi\cdot 10\,\mathrm{kHz}$, $\Omega_\mathrm{m} = 2\pi\cdot 1\,\mathrm{MHz}$, $\kappa = 2\pi\cdot 800\,\mathrm{MHz}$

[21]Here, "standard optomechanical setups" refers to FFPCs where one optical mode interacts with one mechanical mode.

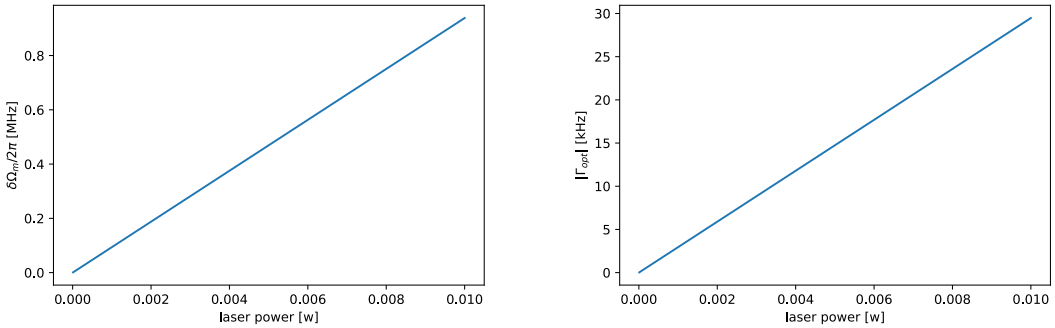

(a) **(b)**

Figure 3.6: Expected values for $\delta\Omega_\mathbf{m}/2\pi$ (a) and $\Gamma_\mathbf{opt}$ (b) as a function of laser power for $g_0 = 2\pi \cdot 10\,\mathrm{kHz}$, $\Omega_\mathrm{m} = 2\pi \cdot 1\,\mathrm{MHz}$, $\kappa = 2\pi \cdot 800\,\mathrm{MHz}$ and $\Delta = 2\pi \cdot 400\,\mathrm{MHz}$.

and $\Delta = 2\pi \cdot 400\,\mathrm{MHz}$, values of the orders of magnitude expected in this project. These values are large enough that both the optical spring effect and optomechanical damping should be observable through this setup. As such, this setup not only enables measurements of mechanical modes but also control of them.

4

Results

In this chapter, the results of the experiments conducted during this master's thesis are presented and discussed.

4.1 Optical characterisation

This section deals with the experimental results obtained with the setup for optical characterisation of FFPCs. This setup was used to analyse reflective properties of FFPCs.

4.1.1 Sweeping of the cavity length

Sweeping the cavity length, by applying a sinusoidally varying voltage on the shear plate actuator, whilst simultaneously measuring the reflection from the FFPC, results in a number of dips in the reflection signal. Recording the voltage applied when these reflection dips occur results in plots like those shown in Figure 4.1. These reflection dips correspond to a resonance between a mode in the FFPC and the laser drive. As such, a data point in Figure 4.1 indicates the voltage necessary to modulate the cavity length such that $\omega_{\text{cav}} = \omega$ for a laser frequency ω. The different types of markers for data points in the plots represent different series of measurements. As shown in Equation 2.1, the length of the cavity has an approximately linear dependence on the wavelength. Measurements of the voltage applied to the shear plate actuator, as exemplified by Figure 4.1, show a corresponding, almost linear, relationship between the wavelength and corresponding voltage at resonance. This indicates that there is an almost linear relationship between the voltage applied on the shear plate actuator and the cavity length. The figure shows several actuator voltages resulting in resonance for every wavelength step. The two lines of data points that are close to each other ($<0.1\,\text{V}$) for the same measurement series are the result of the hysteresis of the shear plate actuator. This hysteretic behaviour makes it so that L_{cav} does not have the exact same dependency on the modulation voltage for the backwards and forwards movements [14]. As such, one of the corresponding reflection dips occurs as L_{cav} increases and one occurs as L_{cav} decreases. The existence of more than one pair of close lines for each series of measurement shows that the shear plate actuator modulates L_{cav} with more than half a wavelength. Therefore, the laser, during one sweep with the fibre mirror back and forth, becomes resonant with more than one longitudinal cavity mode, indicated by the

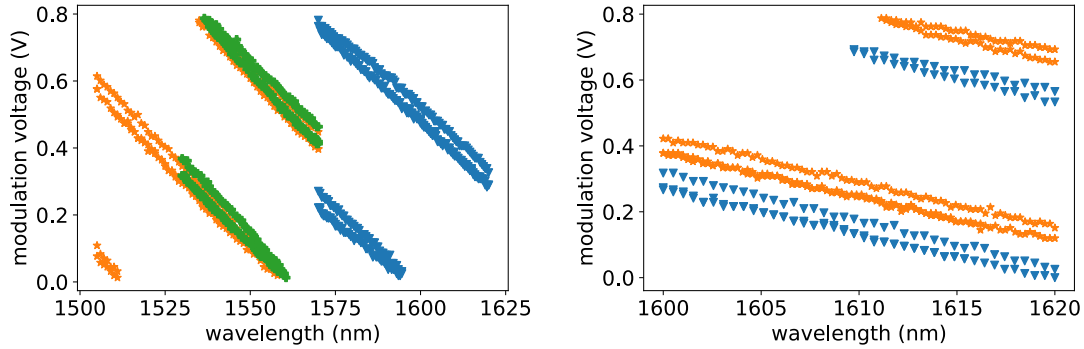

(a) (b)

Figure 4.1: Applied modulation voltage at resonance for a number of wavelengths for two FFPCs consisting of a fibre mirror from LAYERTEC and two different dielectric DBR chips. The different markers in the plots represent different series of measurements. The change in the vertical bias of the voltage profiles between different series of measurements indicates a creep in the mechanics of the setup.

mode number N in Equation 2.1. This means that, for a large enough depth of the reflection dip, one will always see a reflection dip whilst sweeping L_{cav} in this way. Furthermore, it is possible to approximate the free spectral range of the cavity by measuring the horizontal distance between these different groups of lines.

During the different measurement series, indicated by the different marker types in Figure 4.1, the vertical bias of the voltage profiles varies despite the fact that the measurement setup was not changed in between these measurement series. This indicates a creep in the mechanics of the setup which changes the cavity length. This creep could for example be the result of thermal fluctuations in the setup.

4.1.2 Measurements of cavity finesse

Figure 4.2 shows three examples of reflection dips for the same FFPC but for different wavelengths. In all three instances, the sideband frequency applied by the EOM were the same and so was the alignment of the cavity mirrors. As such it is clear that the FFPC had a higher finesse for wavelength 1570 nm than for 1500 nm as the width of the dip, directly proportional to κ, is smaller for 1570 nm. The figure also shows fits of the reflection signals to Equation 3.5. The fit was successful for Figures 4.2a and 4.2b but not for 4.2c. Failure of the fitting algorithm was caused by poor estimations of start parameters, in particular the start parameters for ν_{laser1} and ν_{laser2}. This happened approximately once per 70 wavelengths steps and these measured values for κ could be manually discerned as unreliable by looking at the fit or plotted approximation of the sideband placement. In the future, the fitting algorithm could be improved upon to sort out failed fits automatically.

Figures 4.3, 4.5, 4.6, 4.8 and 4.7 show the measured finesse, $\mathcal{F}$, for different FFPCs as a function of wavelength $\frac{c}{\omega}$. As before, the different markers indicate different

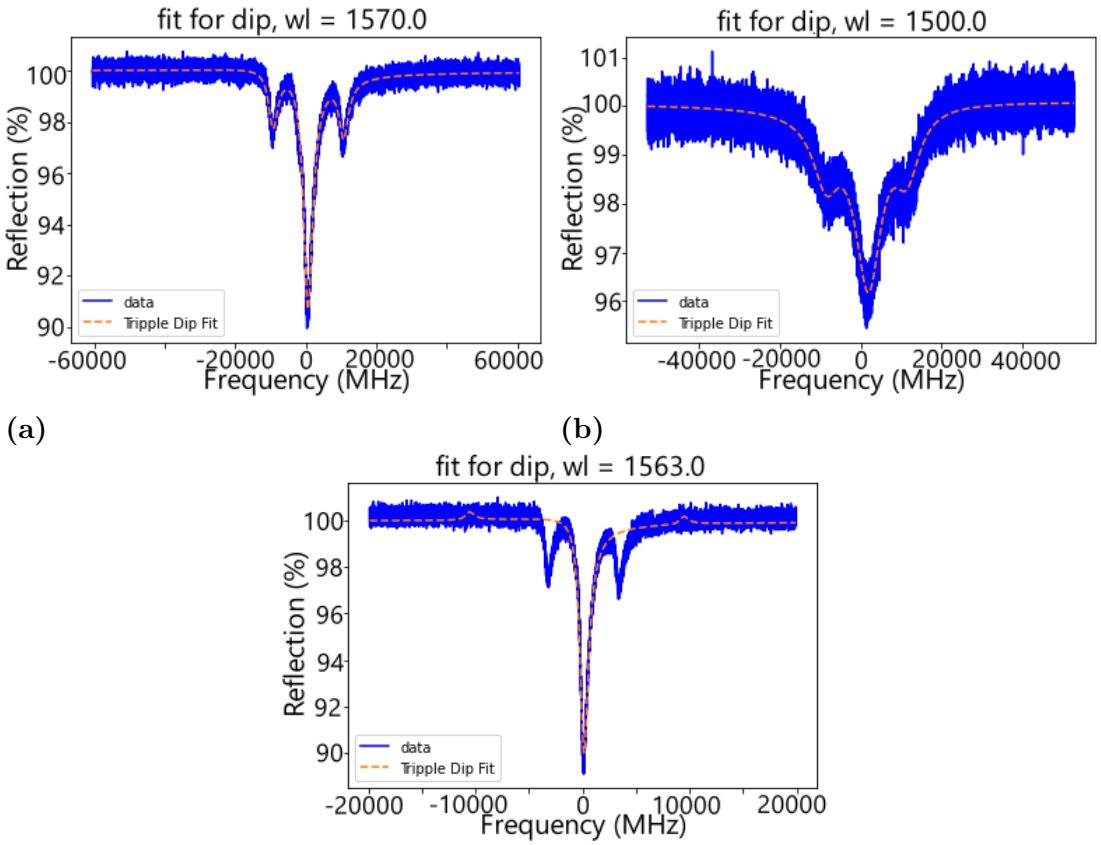

Figure 4.2: Examples of reflection dips fitted to Equation 3.5. The blue graphs indicate the reflected power as recorded by the photodetector whilst the orange dashed lines are the fit of the reflection data to Equation 3.5. The reflection is normalised to the maximum reflection according to the fit.

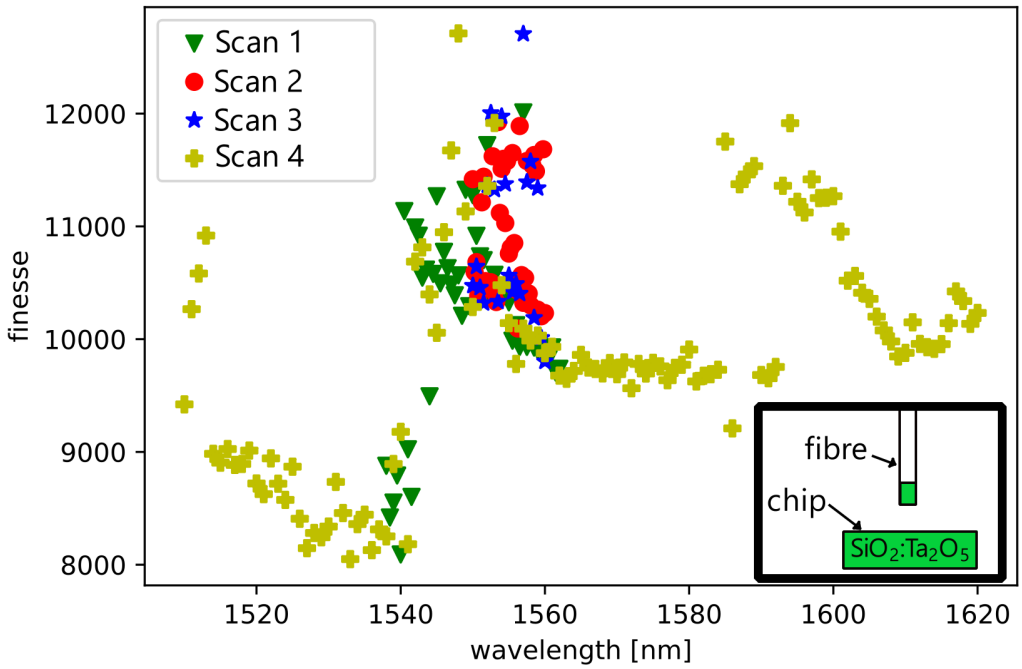

Figure 4.3: Measured finesse for a FFPC consisting of a fibre mirror from LAYERTEC and a macroscopic mirror with the same reflective coating, alternating layers of SiO_2 and Ta_2O_5 of varying thicknesses.

instances of measurement. Figure 4.3 shows the measured finesse for a FFPC consisting of a DBR (distributed Bragg reflector) fibre mirror from LAYERTEC with a macroscopic mirror from LAYERTEC. Both the fibre mirror and the macroscopic mirror had reflective coatings consisting of alternating layers of SiO_2 and Ta_2O_5 of varying thicknesses. Some of the layers of the fiber mirror had been etched away with hydrofluoric acid to decrease reflectivity. Figure 4.4 shows the reflectivity for the fibre mirror before etching according to LAYERTEC. The reflectivity is relatively flat in the wavelength range 1500-1650 nm. The finesse of a FFPC is,

$$\mathcal{F} = \frac{\omega_{\mathrm{FSR}}}{\kappa} = \frac{2\pi}{\mathcal{L}_{\mathrm{tot}}} = \frac{2\pi}{\sum_i (1 - R_i)} \tag{4.1}$$

where $\mathcal{L}_{\mathrm{tot}}$ is the total losses in the system and R_{i} is the the reflectivity of cavity mirror i. Therefore, the finesse is also expected to have a relatively flat response for the same wavelength range. However, that does not appear to be the case in Figure 4.3. $\mathcal{F} \approx \frac{2\pi}{1-R_{\mathrm{fibre}}}$ because the reflection from the macroscopic mirror was much larger than from the fibre mirror. So an increase of finesse from $\mathcal{F} = 8000$ to $\mathcal{F} = 12000$ corresponds to a reflection increase of about

$$\frac{R|_{\mathcal{F}=12000} - R|_{\mathcal{F}=8000}}{R|_{\mathcal{F}=8000}} = \frac{1 - \frac{2\pi}{12000} - \left(1 - \frac{2\pi}{8000}\right)}{1 - \frac{2\pi}{8000}} \approx 0.026\,\% \tag{4.2}$$

which is a very small change and could be the result of roughness or imperfections of the fibre mirror caused by the etching. It is also possible that just the act of removing layers from the fibre mirror through etching changed its properties such

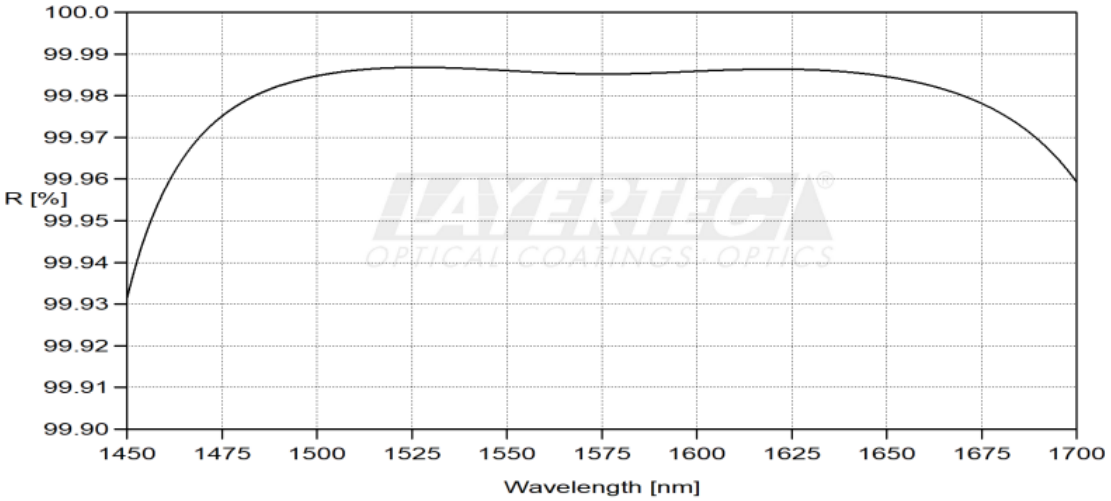

Figure 4.4: Reflectivity of the fibre mirror before etching, taken from the specification sheet from LAYERTEC.

that it has a less flat reflection curve then it did before. Two cavity mirrors with the reflectivity displayed in Figure 4.4 would have a finesse $\mathcal{F} \approx 21000$ for a wavelength of 1575 nm so it is clear that the etching had effect. It is interesting though that the spread of the measured finesse is so large in the range 1540-1560 nm and that the scattering of the Finesse values in this range seems systematic. This discrepancy is not only between different measurements series. The finesse also varies quickly in that range even for the same measurement set. It could be that, for this range of wavelengths, resonances are excited between the layers in the DBRs. How much of these modes are excited could have a strong dependency to the relative alignment between the mirrors and thus would be sensitive to the vibrational noise in the setup. As a result, the finesse value would be more sensitive to the vibrational noise of the setup. The error margins of the measurement scheme need more careful exploration in order to say to which degree this finesse feature is caused by noise in the setup and to which degree it is an inherent property of the cavity mirrors. In order to investigate this one could try different scan speeds. Slow noise processes have a decreasing effect with increased scan speed. One could also explore the hysteresis of the shear plate actuator as that might distort the measured reflection signal. One could also measure the finesse many times for the same wavelength and plot the spread of those values as a function of time.

Figure 4.5 shows finesse measurements for two different FFPCs consisting of a fibre mirror from LAYERTEC and two different dielectric DBRs. The two dielectric DBRs making up the macroscopic mirror in either FFPC are chips made from different parts of a wafer where the composition aimed for was alternating layers of 270 nm silicon dioxide and 111 nm silicon. The reflection coefficient was much lower for the macroscopic mirrors than for the fibre mirror. Therefore, the wavelength dependency of the finesse for these FFPCs can be assumed to be due to the wavelength dependency of the reflectivity from the macroscopic mirrors. For one of the DBRs (see Figure 4.5b) the finesse continued to increase for higher wavelengths throughout

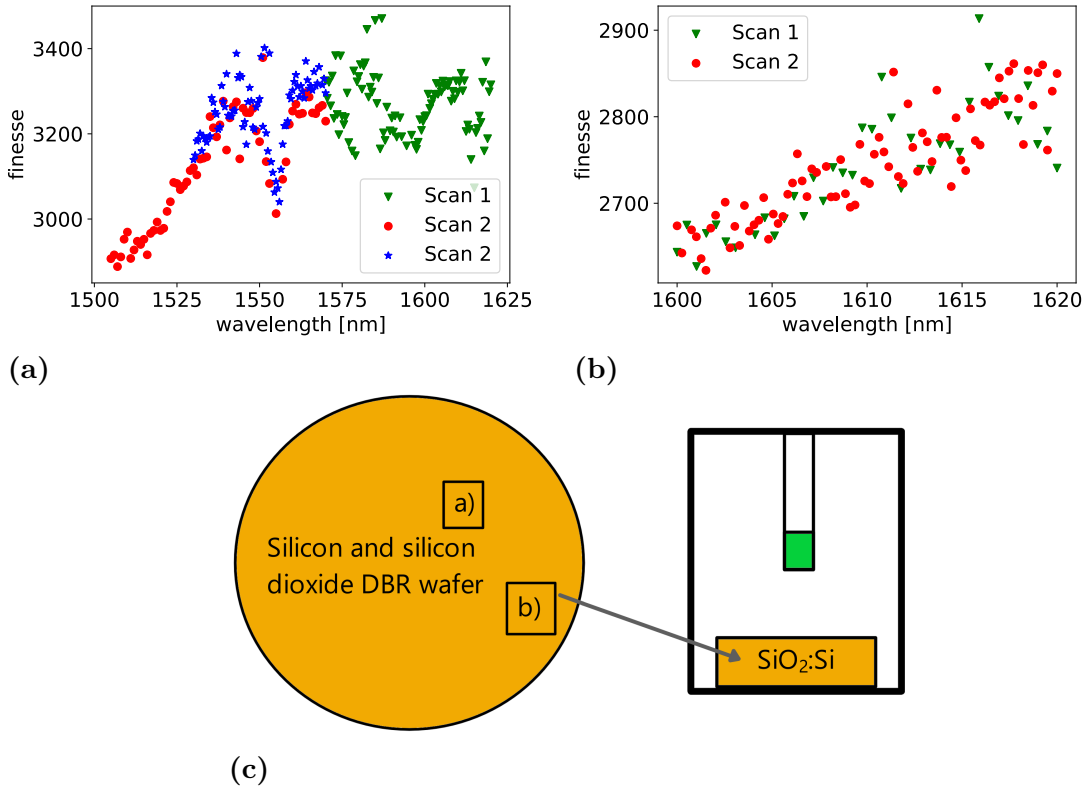

Figure 4.5: Measured finesse for two FFPCs consisting of a fibre mirror from LAYERTEC and dielectric DBRs. The two dielectric DBRs making up the macroscopic mirror in either FFPC are chips made from a wafer with varying layers of 111 nm silicon and 270 nm silicon dioxide. The different markers indicate different series of measurement. c) illustrates the structure of the two FFPCs and indicates where on the DBR wafer the two chips where taken.

the entire wavelength range of the lasers. This indicates that the highest reflection peak for this chip was shifted to outside the laser range probably due to slightly thicker silicon and silicon dioxide layers on that part of the wafer. For the other DBR (see Figure 4.5a), maximum finesse was reached at a wavelength of about 1540 nm after which the finesse approximately flattened out with the exception of a dip at around 1555 nm. Similar to Equation 4.2, this dip in finesse corresponds to a change in reflection with around 0.025 % which is not explained with the theoretical prediction for reflection from the DBR. However, this feature was closely reproduced for two different measurement series so it does not appear to be a measurement error. Perhaps energy is coupled to another optical mode within this wavelength range, for example guided modes of the DBR, which would guide energy away from the cavity. For a plane wave incident perpendicular on an ideal DBR, this would not happen as the k-vector for the plane wave and the k-vectors for the guided DBR modes would be perpendicular. FFPC modes however have more lateral spread in k-space and can therefore couple more easily to modes perpendicular to one of the cavity mirrors. Furthermore, the ideal case for the DBR assumes completely smooth layers which will not be the case for a real DBR. That the behaviour is different for the different DBR chips despite them being made from the same wafer can be explained by uneven thickness of the layers across the wafer.

Figures 4.6, 4.8 and 4.7 show the finesse measured for FFPCs consisting of the fibre mirror in Figure 4.3 and different structures on a chip. Where on the chip those structures were is shown in Figure A.1. Figure 4.6 shows the measured finesse for a FFPC where the macroscopic mirror consisted of a suspended membrane of a photonic crystal made from InGaP patterned with microscopic holes. This membrane was suspended over a thin layer of unpatterned InGaP on top of a DBR consisting of alternating layers of GaAs and AlGaAs as illustrated in the inset of the graph. Outside the wavelength range 1480-1510 nm, the resonance dips were too shallow and the finesse could not be measured which indicates that the finesse outside that range was lower than the finesse inside that range.

Figure 4.7 shows the finesse measured on the same chip but without the suspended photonic crystal membrane. There the structure of the chip was instead a layer of unpatterned InGaP, on top of a layer of GaAs, on top of a thin layer of InGaP, on top of the DBR. In Figure 4.8 the finesse was measured on a part of the chip where the top InGaP layer and the GaAs had been removed. For comparison, Figure 4.9a and 4.9b show the theoretical reflection curve for a Gaussian beam from the photonic crystal simulated with S^4 [15]. Figure 4.10a similarly shows the simulated reflectivity of a Gaussian beam from the DBR with the InGaP layers in the ideal case. The waist for the Gaussian beam was assumed to be 15 μm for both simulations whilst the waist in the FFPCs was estimated to be about 7 μm, this difference is not expected to cause significant change in the reflectivity. The simulation did not take into account the phase of the reflected light which might affect the reflectivity due to constructive and destructive interference. Figure 4.10b shows $\frac{2\pi}{1-R_{\mathrm{DBR}}}$ where R_{DBR} is the reflection coefficient in Figure 4.10a. The reflectivity of the fibre mirror was much higher than the reflectivity of the DBR chip. Because of that, the reflectivity of the fibre mirror did not have much effect on the finesse value in comparison to the effect

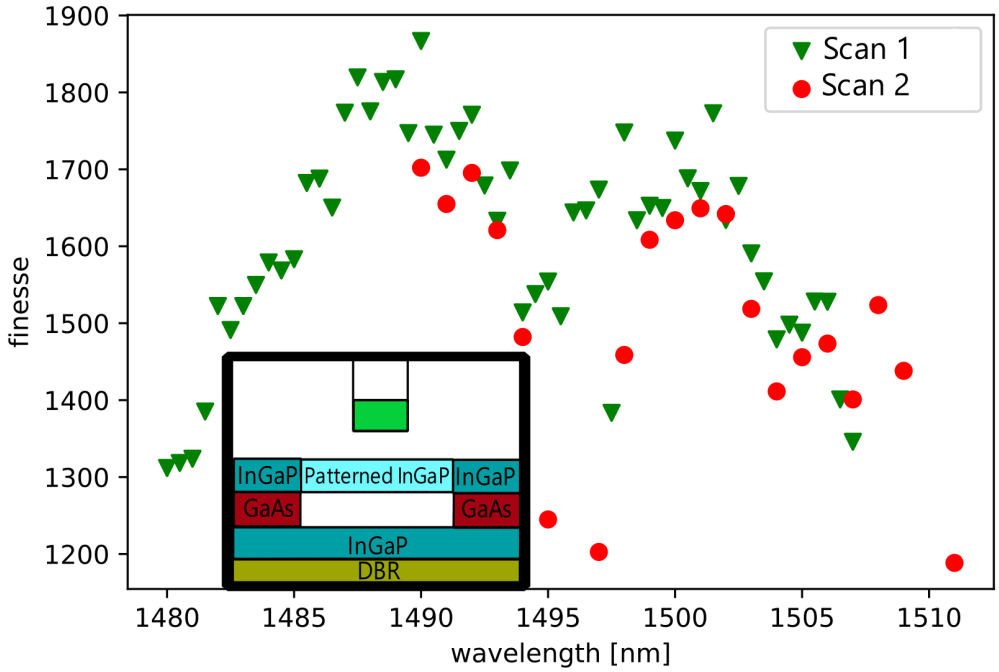

(a)

Figure 4.6: The measured finesse for a FFPC consisting of a fibre mirror from LAYERTEC and a macroscopic mirror, the structure of which is shown in the see inset.

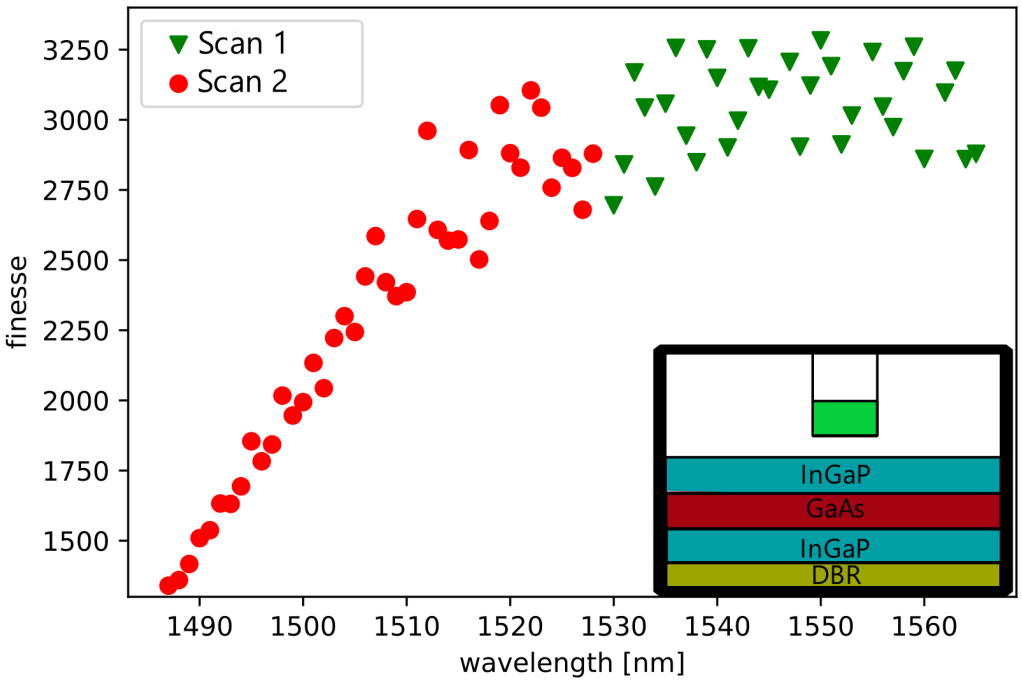

(a)

Figure 4.7: The measured finesse for a FFPC consisting of a fibre mirror from LAYERTEC and a macroscopic mirror, the structure of which is shown in the see inset.

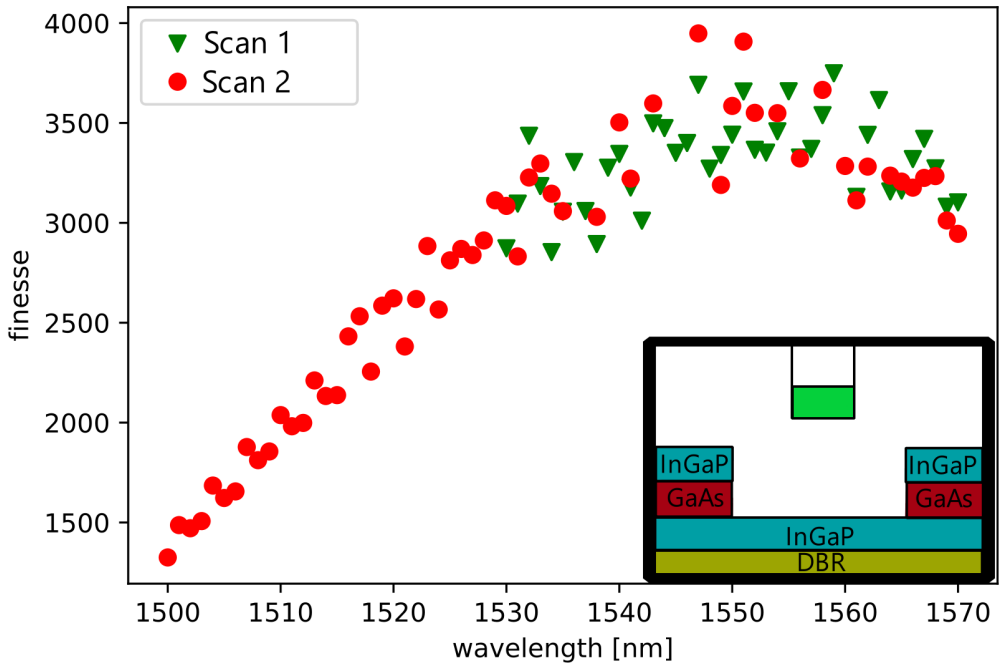

(a)

Figure 4.8: The measured finesse for a FFPC consisting of a fibre mirror from LAYERTEC and a macroscopic mirror, the structure of which is shown in the see inset.

of the DBR chip, see Equation 4.1. Therefore, the finesse for the FFPC, consisting of the fibre mirror and the DBR with the InGaP layers, should in theory be similar to Figure 4.10b. Although, the reflection coefficient in Figure 4.10a represents an ideal case of this DBR, in reality the reflectivity of the DBR was much lower and therefore the actual finesse was also expected to be lower than $\frac{2\pi}{1-R_{\mathrm{DBR}}}$. But the wavelength dependency of $\frac{2\pi}{1-R_{\mathrm{DBR}}}$ and the finesse of the FFPC in Figure 4.7 should in theory be similar and they are. The difference can be explained by slight differences in layer thicknesses, shifting the reflection maxima to a higher wavelength for the real DBR.

The wavelength dependency of the finesse for the photonic crystal on the other hand does not correspond to the simulated reflectivity. This is a more complex system then the other FFPCs explored in this project. The photonic crystal and the DBR underneath form an additional optical cavity. There are also additional modes that energy can couple to in the photonic crystal that are not accounted for in the simple model for the FFPC [16]. As such, $\mathcal{F} \propto \frac{1}{\sum_i (1-R_i)}$ no longer holds as this equation assumes independent reflectivities.

4.1.3 Polarisation dependency of the reflected power

Figure 4.11 shows a series of reflection dips for different wavelengths for an FFPC consisting of the fibre mirror in Figure 4.3 and a DBR consisting of two alternating layers of InGaP and GaAs on top of alternating layers of AlGaAs and GaAs. Several of the panels, for example Figure 4.11b, show two overlapping reflection dips. This

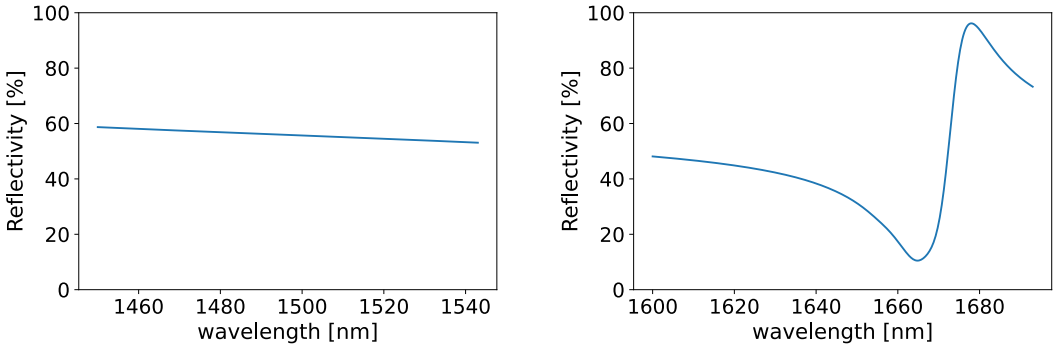

(a) (b)

Figure 4.9: Simulated reflectivities for a Gaussian beam, with waist radius $15\,\mu$m, perpendicular to the photonic crystal structure of the membrane in Figure 4.6

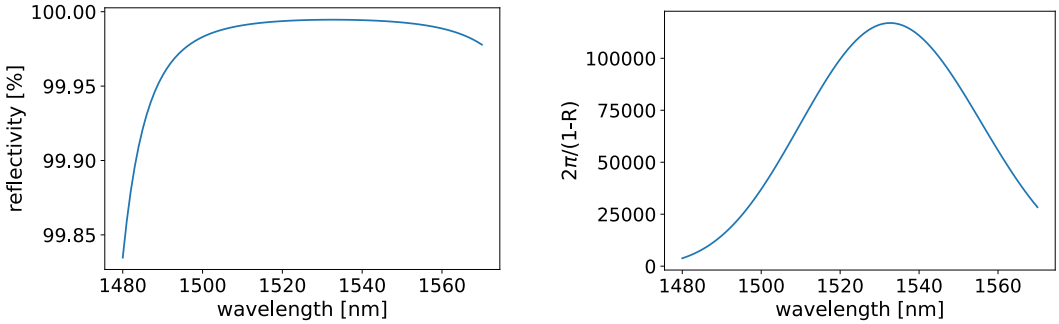

(a) (b)

Figure 4.10: a) shows the simulated reflectivity for a Gaussian beam, with waist radius $15\,\mu$m, perpendicular to the ideal version of the InGaP on DBR structure in Figure 4.7. b) shows $\frac{2\pi}{1-R}$ where R is the reflection coefficient in a).

is because the reflection at the FFPC was polarisation dependent. This was shown by the fact that changing the polarisation of the light entering the FFPC with the paddle wheel polarisation controller shifted the balance between the two peaks, reducing them to a single peak for the right polarisation. This happens because the effective cavity length (including penetration into the mirrors as well as the distance between the mirrors) differs for different polarisations if one or both mirrors are birefringent. The fibre mirror did not cause noticeable birefringence so the double dips here are due to birefringence in the macroscopic mirror. Observing birefringence in strained crystals is not surprising and has been observed for both InGaP [17] and GaAs [18].

The next step to investigate these birefringent properties would be to measure how the fibre changes the polarisation of the light. This can be done by putting a polarisation filter between the facet of the fibre and a photodetector and measuring the power on the photodetector for different wavelengths. This will then make it possible to discern whether the birefringence is wavelength dependent. It is possible that the wavelength dependency observed in 4.11 is because the polarising properties of the fibre are wavelength dependent. Further, one could use sidebands to rescale the x-axis in the reflection plots to frequency as described in Section 3.1.2. The the frequency difference between the two reflection dips could then be used to calculate the difference in refractive index between the two polarisation states. As $\nu_{\text{cav}} \propto \nu_{\text{FSR}}$, see equations 2.1 and 2.2, the fraction between the two frequencies would be

$$\frac{\nu_e}{\nu_o} = \frac{\nu_{\text{FSR},e}}{\nu_{\text{FSR},o}} = \frac{L_{\text{cav effective},o}}{L_{\text{cav effective},e}} = \frac{L_{\text{cav}} + L_{po}}{L_{\text{cav}} + L_{pe}} \tag{4.3}$$

where L_{po} is the effective penetration depth into the DBR chip for one polarisation state and L_{pe} correspondingly for the perpendicular polarisation state. After some algebra this can be expressed as

$$\Delta f L_{\text{cav}} = (f_e - f_o)L_{\text{cav}} = f_o L_{po} - f_e L_{pe} = L_{\text{p,geo}}(f_o n_o - f_e n_e) \tag{4.4}$$

where $L_{\text{p,geo}}$ is the actual, geometric, penetration depth into the chip and n_o and n_e are the refractive indices for the two polarisation states.

4.2 Experiments with the vacuum integrated optomechanical setup

The tests done on the vacuum integrated setup for optomechanical experiments concerned decreasing the noise in the setup to enable PDH and SoF locking, the results of which will be presented in this section. The electrical noise from the RedPitaya was decreased by adding a resistor after the voltage amplifier to act as a low-pass filter together with the capacitance of the shear plate actuator, see Figure 3.5. Without this extra resistor, the reflection signal was distorted too much by the electrical noise. Attempts to lock were made with a 66 kΩ and a 18 kΩ resistor. The lock was more stable with the 18 kΩ resistor indicating that the bigger resistor made the cut-of frequency for the low-pass filter low enough that it inhibited the ability of

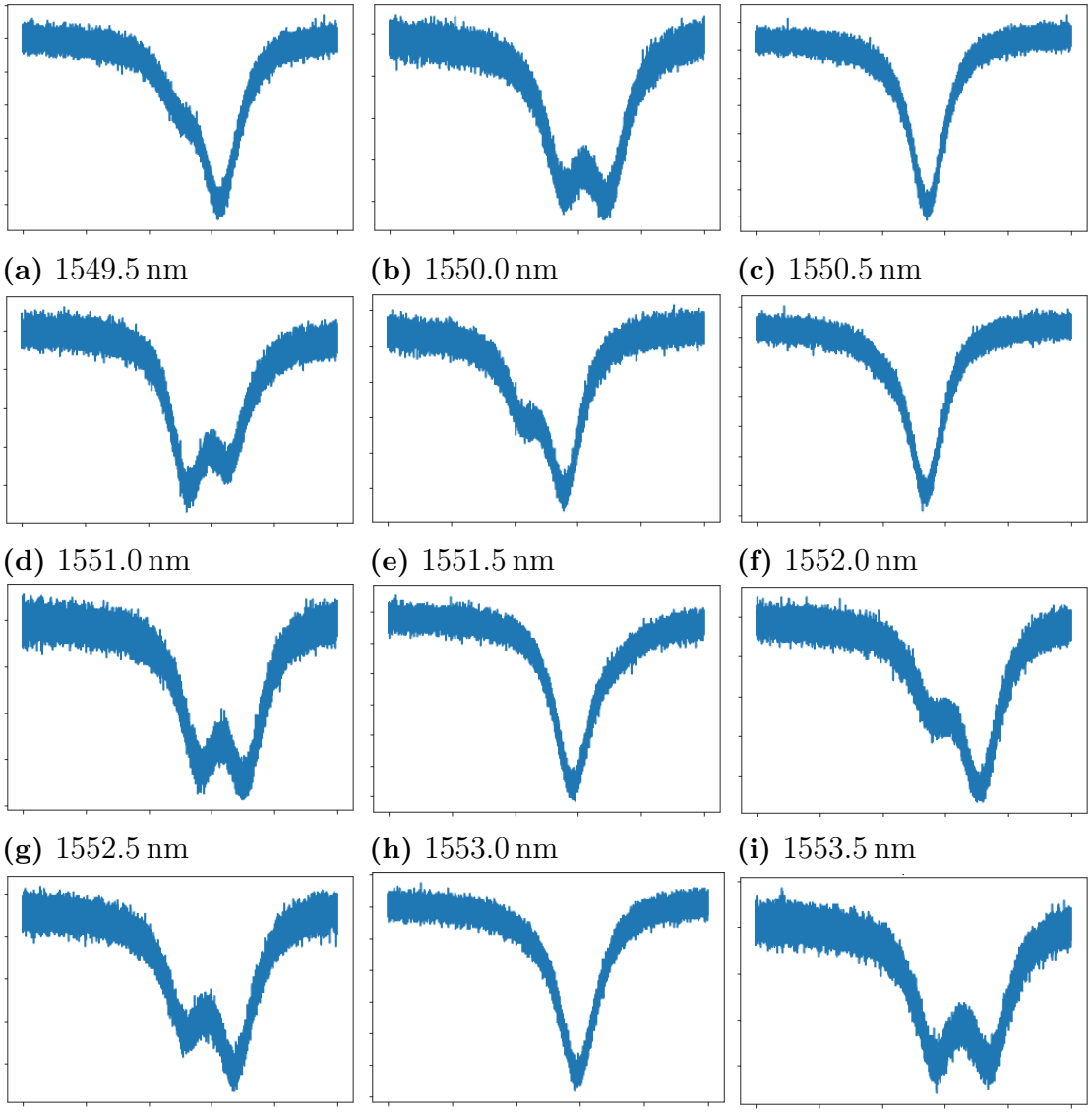

(a) 1549.5 nm **(b)** 1550.0 nm **(c)** 1550.5 nm

(d) 1551.0 nm **(e)** 1551.5 nm **(f)** 1552.0 nm

(g) 1552.5 nm **(h)** 1553.0 nm **(i)** 1553.5 nm

(j) 1554.0 nm **(k)** 1554.5 nm **(l)** 1555.0 nm

Figure 4.11: A series of reflection dips showcasing birefringence in the cavity mirrors. The x-axis is time and the y-axis reflected power, each with arbitrary units. The labels indicate the laser frequency for the corresponding measurement.

the PID controller to compensate for high frequency noise in the system. Attempts were also made to lock with and without the metal springs, see Figure 3.4. Without the springs, locking was not possible as the resonance dip in the reflection signal drifted too much. This indicates the presence of mechanical drift or low frequency oscillations in the setup, causing a change in the cavity length over time. The springs managed to decrease this by creating an additional mechanical connection between the structure holding the fibre mirror and the structure holding the chip mirror. Noise in the reflection signal was further decreased by taping the patch cord fibre to the optical table. The vacuum pump created sinusoidal oscillations in the background reflection signal, inhibiting locking when the pump was on. This can be reduced by turning the vacuum pump off during measurements or by replacing the pumping system with one having lower vibrations.

Figure 4.12 shows the noise spectral density for the error signal, $\mathcal{S}_\epsilon$, of a SoF lock of a FFPC consisting of a fibre mirror and a reflective structure on chip that was not free to vibrate. This measurement was taken before the setup was put into vacuum. The noise is expected to be less in vacuum. The noise that is most relevant for the application is the noise in the frequency range close to the expected mechanical frequencies, $\Omega_\mathrm{m}/2\pi$, of a few MHz. The magnitude of $\mathcal{S}_\epsilon$ in that range needs to be small compared to the additional noise caused by the mechanical resonator motion in order to extract the resonator frequency and g_0 from $\mathcal{S}_\epsilon$ with the help of equations 3.22 and 3.23. That will be the subject of future studies.

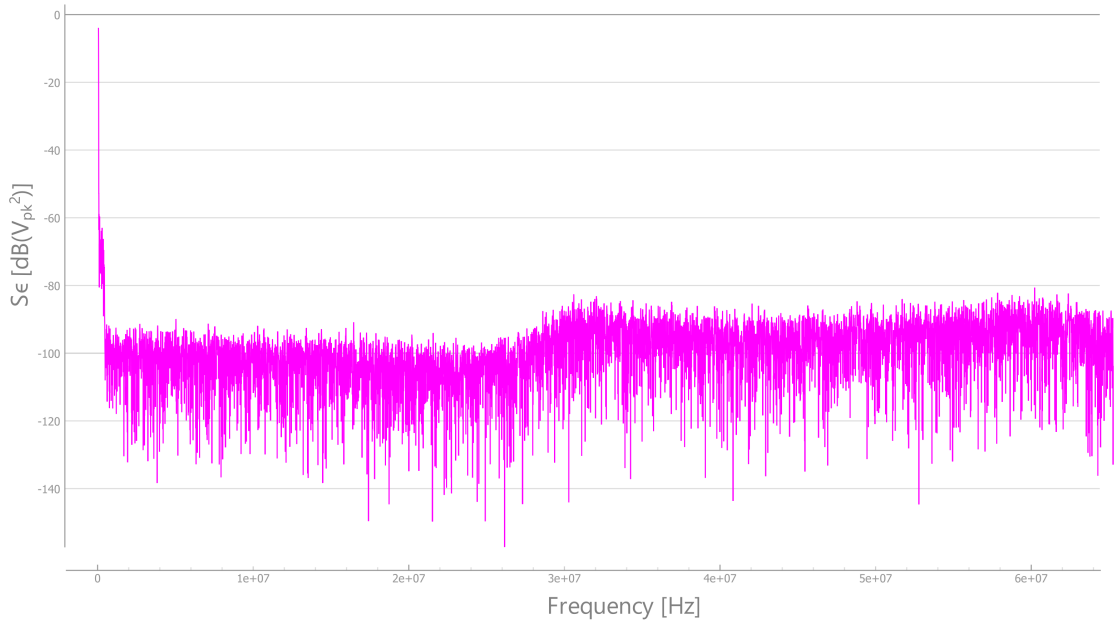

(a)

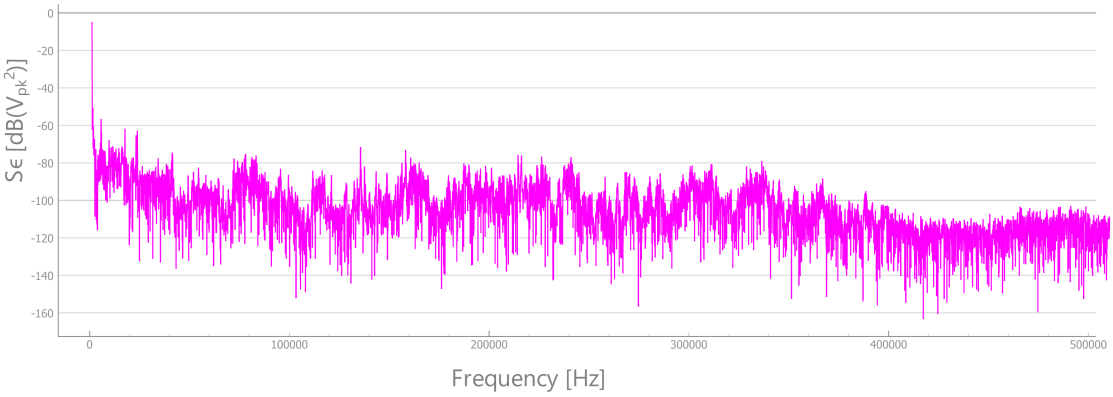

(b)

Figure 4.12: Noise power spectral density of the error signal for a SoF lock of a FFPC for two different noise frequency ranges.

5

Conclusion & Outlook

In this thesis, an experimental platform for optical characterisation of fibre Fabry-Pérot cavities (FFPCs) has been implemented. This setup allows one to study their properties by facilitating measurements with high wavelength resolution. The high wavelength resolution makes it possible to discern small features in the reflectivity spectrum of on-chip structures and fibre mirrors.

The experimental platform has been used to study the reflective properties of a fibre mirror and various reflective on-chip structures, like DBR coatings and photonic crystal structures. The results showed that DBRs consisting of InGaP on top of alternating layers of AlGaAs and GaAs can be birefringent with polarisation dependent properties. The results also demonstrated how small imperfections in fabrication can affect the optical properties of DBRs. For example, chips from the same wafer, and thus theoretically with the same composition, had different reflective properties. Further, the results suggested that the Gaussian mode of a FFPC, consisting of a fibre mirror and a dielectric DBR, can couple to optical modes guided in the DBR leading to additional features in the expected reflection curves of the DBR. The optical properties of a FFPC consisting of a fibre mirror and a photonic crystal suspended over a DBR were examined. The optical properties of that FFPC could not be modelled only by the reflectivities of the fibre mirror and the photonic crystal. This demonstrated that a more complex model is needed to theoretically explain that system, a finding which is consistent with [16]. This experimental platform can in future works be an important tool to facilitate the testing of theoretical models for the reflection from FFPCs with photonic crystals. One could increase the reliability of such measurements by studying the hysteresis of the shear plate actuator and how to better modulate the cavity length to minimise hysteresis-induced distortions of the reflection signal.

Additionally, a vacuum integrated experimental setup was constructed that in future work will be used to conduct optomechanical experiments with FFPCs, allowing optical readout and control of mechanical resonators on chips. Integrating the setup with a vacuum chamber allows for optomechanical experiments without the quality factor of the mechanical resonators being limited by the damping from the surrounding air.

In future work, the vacuum integrated setup will be used for optomechanical experiments with FFPCs consisting of a fibre mirror and photonic crystal mechanical resonators. The small size of the FFPC will allow for small cavity lengths, L_{cav}.

Using photonic crystals will make it possible to achieve smaller effective masses, m_{eff}, of the membranes compared to if one would use for example DBRs. This will make it possible to achieve higher values for the single photon coupling strength g_0 At the same time, FFPCs have been shown to achieve small values for κ [19]. Together, this makes it possible to achieve higher values for $\frac{g_0}{\kappa}$ and approach the strong coupling regime, $g \sim \kappa$, where the optical and mechanical modes hybridise. To achieve this, the reflectivities of the photonic crystals need to be improved in order to reduce κ. The setup for optical characterisation will be a valuable tool in that endeavour.

Bibliography

[1] K. Kustura, C. Gonzalez-Ballestero, A. d. l. R. Sommer, N. Meyer, R. Quidant, and O. Romero-Isart, "Mechanical squeezing via unstable dynamics in a microcavity," *Phys. Rev. Lett.*, vol. 128, p. 143 601, 14 Apr. 2022. DOI: 10.1103/PhysRevLett.128.143601. [Online]. Available: https://link.aps.org/doi/10.1103/PhysRevLett.128.143601.

[2] S. Bose, K. Jacobs, and P. L. Knight, "Preparation of nonclassical states in cavities with a moving mirror," *Phys. Rev. A*, vol. 56, pp. 4175–4186, 5 Nov. 1997. DOI: 10.1103/PhysRevA.56.4175. [Online]. Available: https://link.aps.org/doi/10.1103/PhysRevA.56.4175.

[3] M. Aspelmeyer, T. J. Kippenberg, and F. Marquardt, "Cavity optomechanics," *Rev. Mod. Phys.*, vol. 86, pp. 1391–1452, 4 Dec. 2014. DOI: 10.1103/RevModPhys.86.1391. [Online]. Available: https://link.aps.org/doi/10.1103/RevModPhys.86.1391.

[4] N. E. Flowers-Jacobs *et al.*, "Fiber-cavity-based optomechanical device," *Applied Physics Letters*, vol. 101, no. 22, p. 221 109, Nov. 2012, ISSN: 0003-6951. DOI: 10.1063/1.4768779. [Online]. Available: https://doi.org/10.1063/1.4768779.

[5] H. Pfeifer *et al.*, "Achievements and perspectives of optical fiber fabry–perot cavities," *Applied Physics B*, vol. 128, no. 2, p. 29, Jan. 24, 2022, ISSN: 1432-0649. DOI: 10.1007/s00340-022-07752-8. [Online]. Available: https://doi.org/10.1007/s00340-022-07752-8.

[6] J. Gallego *et al.*, "High-finesse fiber fabry–perot cavities: Stabilization and mode matching analysis," *Applied Physics B*, vol. 122, no. 3, p. 47, Mar. 10, 2016, ISSN: 1432-0649. DOI: 10.1007/s00340-015-6281-z. [Online]. Available: https://doi.org/10.1007/s00340-015-6281-z.

[7] E. D. Black, "An introduction to pound–drever–hall laser frequency stabilization," *American Journal of Physics*, vol. 69, no. 1, pp. 79–87, Jan. 2001, ISSN: 0002-9505. DOI: 10.1119/1.1286663. eprint: https://pubs.aip.org/aapt/ajp/article-pdf/69/1/79/10115998/79_1_online.pdf. [Online]. Available: https://doi.org/10.1119/1.1286663.

[8] SciPy 1.0 Contributors, *Scipy (version 1.15.0)*, 2025. [Online]. Available: https://scipy.org/.

[9] W3Techs, *Toptica python laser sdk (version 3.2.0)*, 2024. [Online]. Available: https://toptica.github.io/python-lasersdk/index.html#toptica-python-laser-sdk-documentation.

[10] PyVISA Authors, *Pyvisa (version 1.15.0)*, 2025. [Online]. Available: https://pyvisa.readthedocs.io/en/latest/#.

[11] L. Neuhaus and S. Deleglise, *Pyrpl (version 0.9.4.0)*, 2017. [Online]. Available: https://pyrpl.readthedocs.io/en/latest/#.

[12] M. L. Gorodetsky, A. Schliesser, G. Anetsberger, S. Deleglise, and T. J. Kippenberg, "Determination of the vacuum optomechanical coupling rate using frequency noise calibration," *Optics Express*, vol. 18, no. 22, pp. 23 236–2346, Oct. 2010. DOI: 10.1364/OE.18.023236. [Online]. Available: https://pubmed.ncbi.nlm.nih.gov/21164665/.

[13] L. Tenbrake, A. Faßbender, S. Hofferberth, S. Linden, and H. Pfeifer, "Direct laser-written optomechanical membranes in fiber fabry-perot cavities," *Nature Communications*, vol. 15, no. 1, p. 209, Jan. 3, 2024, ISSN: 2041-1723. DOI: 10.1038/s41467-023-44490-7. [Online]. Available: https://doi.org/10.1038/s41467-023-44490-7.

[14] R. Yin, B. Xue, E. Brousseau, Y. Geng, and Y. Yan, "Characterizing the electric field- and rate-dependent hysteresis of piezoelectric ceramics shear motion with the bouc-wen model," *Sensors and Actuators A: Physical*, vol. 367, p. 115 044, 2024, ISSN: 0924-4247. DOI: https://doi.org/10.1016/j.sna.2024.115044. [Online]. Available: https://www.sciencedirect.com/science/article/pii/S0924424724000372.

[15] V. Liu and S. Fan, "S^4 : A free electromagnetic solver for layered periodic structures," *Computer Physics Communications*, vol. 183, no. 10, pp. 2233–2244, 2012, ISSN: 0010-4655. DOI: 10.1016/j.cpc.2012.04.026. [Online]. Available: http://www.sciencedirect.com/science/article/pii/S0010465512001658.

[16] S. K. Manjeshwar *et al.*, "Integrated microcavity optomechanics with a suspended photonic crystal mirror above a distributed bragg reflector," *Opt. Express*, vol. 31, no. 19, pp. 30 212–30 226, Sep. 2023. DOI: 10.1364/OE.496447. [Online]. Available: https://opg.optica.org/oe/abstract.cfm?URI=oe-31-19-30212.

[17] R. Wirth, C. Geng, F. Scholz, and A. Hangleiter, "Determination of ordering induced birefringence in (al)gainp," *Journal of Electronic Materials*, vol. 27, no. 3, pp. 122–126, Mar. 1998, ISSN: 1543-186X. DOI: 10.1007/s11664-998-0201-5. [Online]. Available: https://doi.org/10.1007/s11664-998-0201-5.

[18] J. E. Raynolds, Z. H. Levine, and J. W. Wilkins, "Strain-induced birefringence in gaas," *Phys. Rev. B*, vol. 51, pp. 10 477–10 488, 16 Apr. 1995. DOI: 10.1103/PhysRevB.51.10477. [Online]. Available: https://link.aps.org/doi/10.1103/PhysRevB.51.10477.

[19] D. Hunger, T. Steinmetz, Y. Colombe, C. Deutsch, T. W. Hänsch, and J. Reichel, "A fiber fabry–perot cavity with high finesse," *New Journal of Physics*, vol. 12, no. 6, p. 065 038, Jun. 2010. DOI: 10.1088/1367-2630/12/6/065038. [Online]. Available: https://dx.doi.org/10.1088/1367-2630/12/6/065038.

A

Placement of the structures on the photonic crystal chip

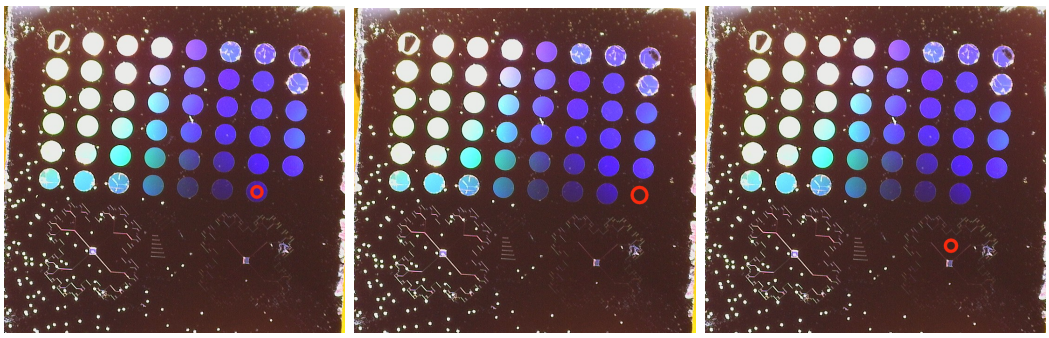

(a) (b) (c)

Figure A.1: Where on the chip with the photonic crystal mechanical resonators that the measurements were taken, marked by the red circle. a) corresponds to the measurement in Figure 4.6. b) corresponds to the measurement in Figure 4.7. c) corresponds to the measurement in Figure 4.8.

DEPARTMENT OF MICROTECHNOLOGY AND NANOSCIENCE
CHALMERS UNIVERSITY OF TECHNOLOGY
Gothenburg, Sweden
www.chalmers.se

CHALMERS
UNIVERSITY OF TECHNOLOGY